Materials
Advances

ROYAL SOCIETY
OF CHEMISTRY

PAPER

View Article Online
View Journal | View Issue

Check for updates

Cite this: *Mater. Adv.*, 2025, **6**, 9085

Fabrication of oxygen vacancy modified 2D–2D g-C_3N_4/$ZnFe_2O_4$ heterostructures for amplifying photocatalytic methyl orange degradation and hydrogen production

Subhasish Mishra,[a] Bhagat Lal Tudu,[b] Nimai Mishra, [c] Kali Sanjay[b] and Rashmi Acharya *[a]

Received 24th May 2025,
Accepted 8th October 2025

DOI: 10.1039/d5ma00533g

rsc.li/materials-advances

2D–2D heterostructured photocatalysts with direct Z-scheme charge dynamics have garnered immense research interest recently owing to their enlarged hetero-interface, which facilitates the separation and migration of photo-induced charge carriers. Although 2D g-C_3N_4 (GCN) and 2D $ZnFe_2O_4$ (ZFO) based photocatalysts have been extensively investigated, the design and performance of GCN/oxygen vacancy-rich ZFO (GCN/O_v–ZFO) 2D–2D heterojunction photocatalysts with Z-scheme charge transfer dynamics remained unexplored. Herein, we reported that the thermal condensation of dicyandiamide (DCDA) with ZFO nanosheets at 550 °C for 5 hours resulted in the formation of GCN/O_v–ZFO 2D–2D heterojunctions. Triethanolamine (TEA) acted as both a complexing agent and a soft template during the synthesis of ZFO nanosheets. Scavenging experiments, XPS results and band-edge potential calculations revealed the formation of a direct Z-scheme charge transfer dynamics. GCN/O_v–ZFO2 displayed a maximum MO degradation efficiency of 99.54% which is 3.7 and 1.8 times higher than that of pristine ZFO and GCN, respectively. It also demonstrated elevated photocatalytic H_2 production of 735.4 μmol g^{-1} h^{-1}, surpassing those of pristine ZFO and GCN by factors of 8.5 and 3.6, respectively. The augmented performance of GCN/O_v–ZFO2 might be attributed to maximized charge separation, extended visible light absorption, improved surface properties and strong redox ability resulting from the combined effect of the 2D–2D heterointerface, introduction of O_vs, and the direct Z-scheme heterojunction.

1. Introduction

Global energy consumption is anticipated to increase by more than 50% in 2040 as a result of the population explosion and the corresponding growth of the industrial, residential, and commercial sectors. With the growing demand for energy and the ensuing environmental concerns, it is imperative to find sustainable and environmentally acceptable alternatives to fossil fuels.[1–3] Hydrogen is regarded as the most advanced possible contender for future energy supply due to its high gravimetric energy density and large calorific value as well as clean combustion product (H_2O).[4,5] Currently, industrial hydrogen production is carried out using coal gasification, steam reforming of natural gas, and partial oxidation of hydrocarbons.[6,7] Although these technologies are being extensively applied, energy expensiveness and greenhouse gas emissions from fossil fuels remain as the shortcomings. On the other hand, excessive reliance on organic dyes in the textile, paint and cosmetic industries causes several health problems in the human body.[8,9] For instance, the robust quinoid and azo structures of the methyl orange (MO) dye can cause skin rashes, cardiac problems, and respiratory issues.[10,11] Nevertheless, poor stability, low efficiency and the generation of secondary pollutants limited the application of conventional methods for the removal of MO.[12] Thus, building a green, sustainable, and economical method for hydrogen production and degradation of organic dyes like MO is peremptorily required.

Visible light responsive semiconductor photocatalysis is regarded as an efficient approach for addressing energy demands and environmental concerns due to its eco-friendliness and economic advantages. The photocatalytic process involves redox reactions over a semiconductor surface using two of the most abundantly available precursors, water and sunlight. Most importantly, the photocatalytic process

---

[a] *Department of Chemistry, I.T.E.R., Siksha 'O' Anusandhan deemed to be University, Bhubaneswar, Odisha 751030, India. E-mail: rashmiacharya@soa.ac.in, drrashmiacharya75@gmail.com; Fax: +91-674-2350642; Tel: +91-674-2350181, +91-674-2351538*

[b] *Hydro & Electrometallurgy Division, CSIR-Institute of Mineral and Materials Technology (IMMT), Bhubaneswar 751013, Odisha, India*

[c] *Institute of Chemical Technology Mumbai, IOC Odisha Campus Bhubaneswar, Bhubaneswar, Odisha, India*

forms harmless secondary products, making this process environmentally benign and sustainable.[13,14] Utilization of dye contaminated waste water can be an economical approach for the photocatalytic production of H_2 energy.[15,16] However, the presence of dye molecules in waste water imparts a wide range of environmental issues.[17] Therefore, it is required to eliminate the organic dyes completely through photocatalytic degradation, followed by producing H_2 energy from the same waste water source. This will make the photocatalytic process inexpensive for both environmental remediation and sustainable energy generation. This diversified application of coupling photocatalytic hydrogen evolution and organic degradation with the same catalytic system could offer noteworthy economic and environmental benefits. In recent years, GCN has garnered the most attention as a catalyst for divergent photocatalytic applications owing to its 2D morphology, metal-free nature, π-conjugate structure, adequate theoretical specific surface area, visible light response, highly negative conduction band position, inexpensiveness and improved thermochemical stability. Its easily accessible precursors, straightforward synthesis process and non-toxicity have also contributed to its widespread application in photocatalysis.[18–20] However, in practice, bare GCN possessed slow exciton transfer kinetics with substantial recombination of electron–hole pairs, a relatively narrow visible-light sensitivity and low surface area, which cumulatively reduce its quantum efficiency significantly.[21] Additionally, the less positive VB level of GCN is inadequate to carry out the water oxidation reaction (WOR) for the production of hydroxyl radicals, which are used as a strong reactive species in photocatalytic degradation. In order to overcome these shortcomings, two-dimensional (2D) GCN can be integrated with a strongly oxidative semiconductor of narrow band gap energy to construct direct Z-scheme heterojunctions. The designed hetero-structure can inhibit electron–hole pair recombination through their spatial separation, render a red shift in the visible light absorption range and make available charge carriers with strong redox ability.[22,23] In this context, ZFO is considered an appropriate material to be coupled with GCN owing to its non-toxicity, structural stability, high dispersibility, matched band-positions with GCN and a narrow bandgap that can upscale the visible light absorption of the heterojunction.[24–26] Attempts have been made to couple GCN with ZFO for favourable photocatalytic applications. For instance, Li *et al.* have prepared a $ZnFe_2O_4$/g-C_3N_4 heterojunction for photo-degradation of methylene Blue (MB), methyl Orange (MO) and rhodamine B (RhB).[27] The Ding group has also put forth a 0D–2D combination of $ZnFe_2O_4$ and g-C_3N_4 for upgraded adsorptive and photocatalytic uranium(VI) removal.[28] However, the 0D–2D interface allows only point-to-face contact that restricts the interfacial charge transfer into a narrow space, and hence, the full potential of the prepared heterojunction could not be achieved.[29,30] In contrast, a 2D–2D heterojunction reduces the interfacial charge transmission path, which consequently decreases the charge transfer resistance. This process accelerates the charge migration and subsequently results in diminished recombination of charge carriers. Additionally, 2D–2D nano hetero-structures significantly enhance the specific surface area, providing an ample amount of exposed active sites for photocatalytic reactions.[31,32] Inspired by such overwhelming benefits, several research groups have fabricated various g-C_3N_4 based 2D–2D heterojunctions for photocatalytic applications. Qin *et al.* have prepared a 2D–2D $ZnIn_2S_4$/g-C_3N_4 van der waals heterojunction for photocatalytic hydrogen evolution. The prepared heterojunction exhibited 6095.1 μmol h^{-1} g^{-1} of H_2 production, which is primarily attributed to the strong electronic interaction resulting from the extended contact interface at the 2D/2D VDW heterojunction.[33] Similarly, an Ag-loaded h-MoO_3/g-C_3N_4 2D–2D heterostructure has been fabricated by Kumaravel *et al.* The prepared composite exhibited 99% of the MB dye and 90% of tetracycline degradation within 1 hour of solar exposure. The robust contact interface triggers the adequate separation of photogenerated electrons that has led to augmented activity.[34]

Downscaling bulk $ZnFe_2O_4$ to a two-dimensional morphology results in unique physicochemical traits, including an increased surface-to-volume ratio and quantum confinement effects.[35] These features expose more active sites and allow for customizable electronic band structures, which significantly boost the reactivity. These characteristics make 2D ZFO extremely useful in photocatalysis and gas sensing applications. Zhan *et al.* demonstrated superior dye degradation performance of hydrothermally prepared ZFO nanoplates owing to their increased surface area, high crystallinity, and plate-like structure.[36] Similar to this, porous ZFO nanosheets improved gas sensing by encouraging quick gas molecule adsorption and diffusion, which improves sensitivity and shortens the reaction time.[37] However, these fabrication techniques involve complex instrumentation and lengthy reaction processes. Therefore, the formation of 2D ZFO should be carried out using simple top-down methods like sol–gel, using a single chemical reagent as a complexing agent and a template. This will shorten the reaction time, avoid the use of multiple reagents and provide required control over the particle morphology.

Triethanolamine is an environmentally friendly, cost effective polydentate organic ligand that offers advantages as a complexing agent and a template for the synthesis of morphology controlled 2D nanomaterials.[38,39] TEA's ability to donate electrons through its nitrogen and oxygen atoms allows it to bind with metal ions *via* multiple point attachment that creates stable and well defined complexes. By complexing with metal ions, TEA can prevent their rapid precipitation, resulting in a more homogeneous solution and controlled growth of the crystals. Additionally, owing to its structure directing properties, TEA can act as a template to control the size, shape, and morphology of nanostructures. However, the potential of TEA in the synthesis of 2D ZFO nanosheets has been rarely reported.

Defect engineering can be applied to deliberately tailor and enhance material's properties for specific applications. Previously, a number of research articles have reported that the photocatalytic activity of 2D metal oxides can be enhanced by incorporating oxygen vacancies.[40,41] The formation of oxygen vacancies in the spinel ZFO was proven to be beneficial for not only escalating charge separation but also the light absorption properties of pristine ZFO. Additionally, these vacancies could enhance the adsorption of pollutant molecules and water for better activity of the material. However, 2D ZFO incorporated with oxygen vacancies has not yet been reported. Furthermore, to the best of our knowledge, the merits of O_v rich 2D ZFO based heterojunctions for achieving augmented photoactivity are yet to be explored.

Inspired by the overwhelming benefits of O_v rich 2D ZFO and 2D GCN, efforts were made to construct novel 2D–2D GCN/O_v–ZFO heterojunctions by employing a strategic two-step approach and to investigate their photocatalytic performances in the present work. First, ZFO nanosheets were synthesized *via* pyrolysis of the precursor obtained from the sol–gel technique using TEA as a complexing agent and a template. The polydentate nature of TEA promotes the controlled hydrolysis of the metal ions to form the metal hydroxides, whereas the structure directing properties of TEA guide the nucleation and further growth of ZFO nanosheets during pyrolysis. In the next step, the GCN precursor (DCDA) along with ZFO nanosheets were subjected to thermal treatment at 550 °C to form a GCN/O_v–ZFO heterojunction. SEM, TEM, and HRTEM analyses have validated the formation of GCN and ZFO as nanosheets and 2D–2D heterojunction construction. Additionally, the high-temperature thermal treatment introduced oxygen vacancies in ZFO, validated by XPS analysis. The 2D–2D heterojunction construction, along with direct Z-scheme charge dynamics, enhanced the charge separation while maintaining high redox potential. The surface vacancies not only provide ample surface active sites but also upscale the light absorption by creating mid-gap energy states. The as-prepared catalysts were successfully applied for photocatalytic hydrogen production and MO degradation under visible light illumination. Finally, based on scavenging experiments, band edge values, and XPS results, a plausible photocatalytic mechanism was proposed. This work provides insightful information for the rational design of morphology-optimized heterojunctions with vacancy engineering towards photocatalytic energy generation and environmental remediation.

2. Experimental

2.1. Chemicals

Zinc chloride ($ZnCl_2 \cdot 6H_2O$), ferric chloride ($FeCl_3$), triethanolamine (TEA) [$C_6H_{15}NO_3$], potassium hydroxide (KOH), ethanol, dicyandiamide (DCDA) [$C_2H_4N_4$], methyl orange ($C_{14}H_{14}N_3NaO_3S$), benzoquinone ($C_6H_4O_2$), and isopropyl alcohol (C_3H_8O) used in this experiment were of analytical grade and were purchased from Merck Co. India.

2.2. Synthesis of $ZnFe_2O_4$ (ZFO)

To prepare pure ZFO, 0.68 g of $ZnCl_2 \cdot 6H_2O$ and 1.62 g of $FeCl_3$ were added to 100 mL of deionised water and the mixed solution was stirred continuously for one hour. 4.1 mL of TEA was added to the metal chloride solutions and was kept stirring for another hour at room temperature. Then, 6 molar KOH solution was slowly added to attain supersaturation and subsequently a brown-coloured gel was formed. The gel was then dried for 24 hours at 80 °C inside a hot air oven. In the next step, the yield was collected in a crucible and calcined at 550 °C for 5 hours in a muffle furnace to obtain ZFO.

2.3. Synthesis of the $ZnFe_2O_4$/g-C_3N_4 (GCN/O_v–ZFO) 2D–2D heterojunction

The as-prepared ZFO was mixed with different amounts of DCDA to formulate a GCN/O_v–ZFO nanocomposite. To a specific amount of bare ZFO, 5 g of DCDA powder was mixed and ground for 30 minutes. The powder mixture was then calcined at 550 °C for 5 hours. The synthesized sample was labeled as GCN/O_v–ZFO1. A similar approach was followed to fabricate GCN/O_v–ZFO2 and GCN/O_v–ZFO3 using 7.5 and 10 g of DCDA, respectively. Pristine GCN was prepared by following an identical procedure without the addition of ZFO. Scheme 1 illustrates the major steps involved in the synthesis process.

2.4. Instrumentation

We utilized a Rigaku Miniflex X-ray diffractometer (100 mA, 40 kV) with Cu Kα radiation (λ = 1.54 Å) for analyzing the crystal structures of the prepared catalysts. The surface chemistry information was obtained using a Buker alpha II spectrophotometer *via* Fourier transform infrared (FTIR) analysis in the wavenumber range of 4000–400 cm^{-1}. X-ray photoelectron spectroscopy (XPS) (ULVAC PHI/PHI5000 Versa Probell) was carried out to identify the chemical environment of each element contained in the samples. The microstructure and morphology were examined using a JEM-F-200 high resolution transmission electron microscope (HRTEM) and a Carl Zeiss Evo 18 scanning electron microscope (SEM). The optical properties of the catalysts were measured using a UV-vis spectrophotometer (JASCO V-750). With an excitation wavelength of 380 nm, a JASCO-FP-8300 spectrofluorometer was used to acquire the photoluminescence spectra. Following five hours of degassing the samples at 300 °C, the materials' BET surface area was measured using a Quantachrome Novae 2200 N_2 adsorption–desorption apparatus. The average crystallite size of ZFO and GCN/O_v–ZFO2 was estimated from the XRD data using the Scherrer equation

$$D = \frac{K\lambda}{\beta \cos\theta} \tag{1}$$

where, D is the average crystallite size, K is the shape factor ($\sim$0.9), λ is the X-ray wavelength, β is the full width at half maximum (FWHM), and θ is the the Bragg angle.

To find the lattice microstrains of the respective crystal lattices, Williamson–Hall (W–H) plot was obtained according to the equation

$$\beta \cos\theta = 4\varepsilon \sin\theta \frac{K\lambda}{D} \tag{2}$$

The lattice microstrain (ε) is calculated from the slope of the W–H plot.

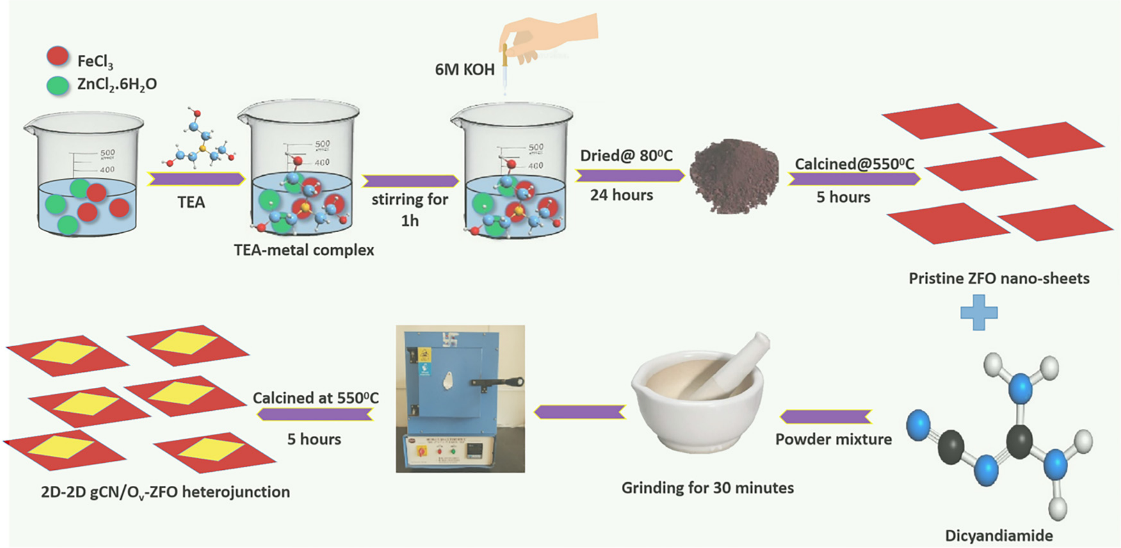

Scheme 1 Schematic representation of the detailed synthesis protocol for the GCN/O$_v$–ZFO heterojunction.

Finally, the lattice constants of both the crystal structures have been calculated by using the following equation

$$\alpha = \frac{\lambda}{2}\sqrt{\frac{h^2 + k^2 + l^2}{\sin^2\theta}} \qquad (3)$$

Here h, k and l represent the Miller indices of the respective crystal facets.

2.5. Photocatalytic activity assessment

To evaluate the photocatalytic efficacy of the obtained catalysts, MO degradation and hydrogen production experiments were performed. The MO photo-degradation experiment was carried out with 50 mL of MO solution (15 mg L^{-1}) containing 20 mg of the catalyst. At first, the pollutant solution with the catalyst was kept in the dark with starring for 30 minutes to establish absorption–desorption equilibrium. Subsequently, the degradation experiments were performed under visible light illumination for 60 minutes. After the completion of this reaction, the photocatalysts were separated from the solution with the help of a centrifuge. The MO concentration in the solution was determined using a UV-visible spectrophotometer (Systronic 2202) at 464 nm.

The photocatalytic MO degradation efficiency was calculated using the following expression.

$$\%\,\text{MO degradation} = \frac{C_0 - C_t}{C_0} \times 100 \qquad (4)$$

where C_0 is the initial MO concentration and C_t stands for the concentration of MO at time t minutes. The reaction kinetics for MO photo-degradation over the prepared catalyst was calculated using the Langmuir–Hinshelwood kinetic model

$$-\ln\frac{C_t}{C_0} = kt \qquad (5)$$

The hydrogen production efficiency of the prepared materials through photocatalytic process was examined using a Lelesil flexi-5D gas photochemical reactor equipped with a 250 W xenon lamp. To be precise, 25 mg of the catalyst was added to 50 mL of 10% aqueous methanol solution and subjected to photocatalytic treatment inside the reactor for 1 hour. The evolved gas was then quantified. The photocatalytic hydrogen production experiments were carried out by following a similar procedure to that reported in our previous works.[42,43]

2.6. Electrochemical characterization

The electrochemical studies of the prepared samples were carried out using a three electrode setup with the help of an electrochemical analyser. In this study, a 0.1 Molar aqueous solution of sodium sulphate (Na$_2$SO$_4$) was used as an electrolyte solution (pH = 6.8). Ag/AgCl was applied as the reference electrode, Pt as the counter electrode and the photocatalyst coated with FTO (fluorine doped tin oxide) conducting glass was employed as the working electrode to carry out all the electrochemical experiments.

3. Results and discussion

3.1. Phase and structure

The structural characterization and phase identifications were carried out using the XRD technique, and the diffraction peaks are illustrated in Fig. 1(A). The characteristic peaks of GCN at 2θ values of 13.0° and 27.4° correspond to the (100) and (002) crystal planes, respectively, of graphitic carbon nitride (JCPDS #87-1526). The (100) plane represents the aromatic network of the tri-*s*-triazine structure, whereas the (002) plane reflects the inter-layer stacking between GCN layers.[44] The formation of cubic ZFO was confirmed by the appearance of the distinct peaks at 29.8°, 35.4°, 42.7°, 53.9°, 56.4° and 62.4° of the (220), (311), (400), (422), (511) and (440) crystal planes, respectively (JCPDS #89-1010).[45] The sharp and intense peaks indicated the higher crystallinity of the prepared ZFO. This is due to the formation of metal–TEA complexes by the chelating action of

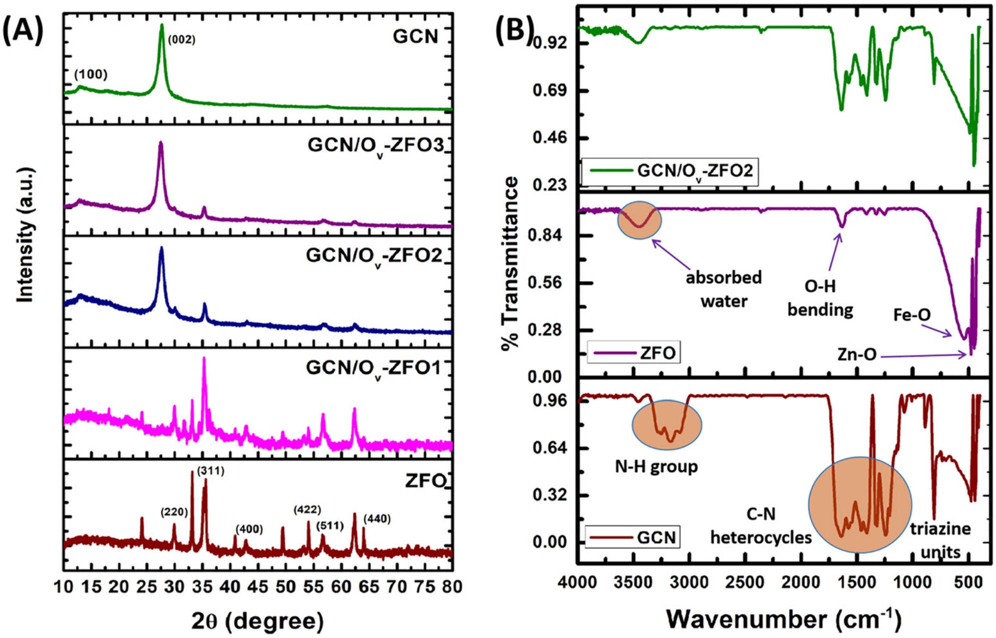

Fig. 1 (A) X-ray diffraction peaks of the as-prepared samples and (B) FTIR spectra of GCN, ZFO and GCN/O$_v$–ZFO2.

TEA. These metal–TEA complexes are more reactive and decompose completely at lower temperatures compared to the metal precursors without TEA.[46] The controlled thermal decomposition process facilitated by TEA helps in the formation of highly crystalline ZFO with better phase purity, meaning fewer impurities and a more uniform crystalline structure. Notably, the X-ray diffractogram of the GCN/O$_v$–ZFO1 composite only displayed the ZFO phase; the characteristic peak of GCN was not visible in any appreciable intensity, most likely because of its low content. The XRD patterns of GCN/O$_v$–ZFO2 and GCN/O$_v$–ZFO3 exhibited all the characteristic peaks for GCN and ZFO. Interestingly, with increasing GCN : ZFO ratio, the characteristic GCN peaks became more apparent while ZFO peaks gradually weakened. The substantial change in the peak intensities specified the sturdy interaction between ZFO and GCN that leads to the formation of a pure phase GCN/O$_v$–ZFO heterojunction.[47]

Furthermore, changes were observed in the characteristic (311) peak of ZFO in GCN/O$_v$–ZFO heterojunctions. The peak experienced broadening and was shifted to a higher 2θ value in the prepared composites as shown in Fig. S1. This might be attributed to the changes in the lattice structure of ZFO in the GCN/O$_v$–ZFO heterostructure. To verify this, the crystallite size and lattice microstrain of the pristine ZFO and GCN/O$_v$–ZFO2 were calculated. The crystallite size was found to be decreased from 24.75 nm to 15.23 nm in GCN/O$_v$–ZFO2. This decrease could be ascribed to an increase in the lattice microstrain. It was observed that the microstrain has increased from 0.34 in ZFO to 0.46 in GCN/O$_v$–ZFO2. The XRD peak broadening, smaller crystallite size and larger microstrain of ZFO in GCN/O$_v$–ZFO indicated the existence of crystal defects that might be associated with the rearrangement of cations within the crystal lattice.[48,49] Furthermore, the lattice parameters of ZFO crystals before and after composite formation have been calculated. A decreasing trend in the lattice parameter from 8.448 Å to 8.437 Å has been observed, suggesting the contraction of the lattice. As per the literature, the high-temperature thermal treatment causes cation disorder in ZFO.[50] The contraction of the lattice cell is ascribed to the migration of Zn^{2+} (having a larger ionic radii compared to Fe^{3+}) from tetrahedral sites to octahedral sites. When Zn^{2+} moves to the octahedral position, it encounters a significant struggle to hold two more oxygen atoms firmly, resulting in the formation of oxygen vacancies. Similarly, the migration of Fe^{3+} from the octahedral to tetrahedral coordination state can disrupt the existing charge balance of the crystal lattice. To compensate it, oxygen ions may leave the crystal lattice, creating oxygen vacancies. This illustration can be used as preliminary evidence for the cation exchange and the presence of oxygen vacancies in the GCN/O$_v$–ZFO heterojunction, which will be further confirmed through XPS analysis.

FTIR spectroscopy was utilized to investigate the chemical environment of the prepared samples, and the results are shown in Fig. 1(B). For GCN, several peaks have been observed in the absorption range of 1150–1700 cm^{-1} related to the stretching mode of the repeated heptazine ring. The C=N bond stretching vibration is represented by the cluster of peaks located between 1557 and 1645 cm^{-1}, whilst the C–N stretching mode is represented by the peaks centered between 1263 and 1416 cm^{-1}. A broad band that appeared between 3000 and 3300 cm^{-1} suggested that hydrogen bonded N–H groups are formed as a result of partial condensation. Additionally, the breathing mode of the triazine units of C–N heterocycles accounts for the vibrational frequency peak at 812 cm^{-1}, which

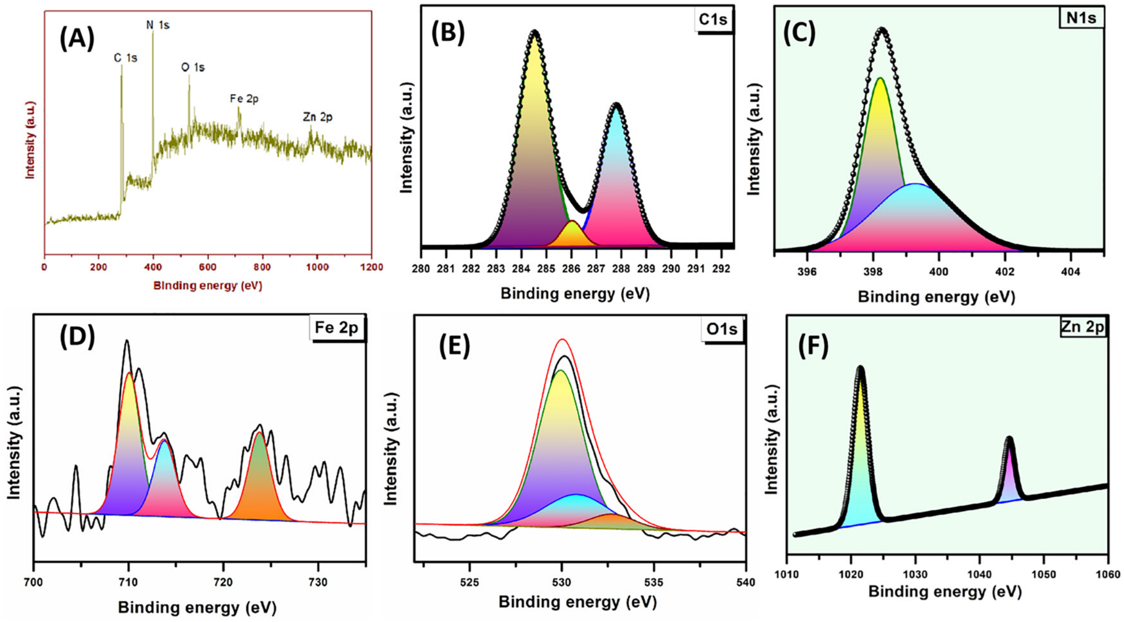

Fig. 2 (A) XPS full survey and high resolution (B) C 1s, (C) N 1s, (D) O 1s, (E) Fe 2p and (F) Zn 2p spectra of GCN/O_v–ZFO2.

is a significant peak for g-C_3N_4.[51] For pristine ZFO, the peak corresponds to the stretching vibration of Zn–O, which appears at 432 cm^{-1} and the peak at 563 cm^{-1} is attributed to the Fe–O bond stretching mode. Additionally, the vibrational frequencies detected at 1635 and 3420 cm^{-1} are associated with the bending and stretching vibrations, respectively, of the O–H groups present on the ZFO surface.[52] The appearance of vibrational modes at 812, 1263, 1416, and 1557 cm^{-1}, as well as that at 563 and 432 cm^{-1} in the FTIR spectrum of GCN/O_v–ZFO2, validated the presence of both GCN and ZFO in the nanocomposite.

The XPS survey spectrum of GCN/O_v–ZFO2 was recorded and shown in Fig. 2(A). From the figure, C, N, O, Fe and Zn elements were confirmed to be present in the sample without any impurities. In order to validate the presence of GCN and ZFO in the fabricated heterojunction, high resolution XPS spectra were recorded. Fig. 2(B) illustrates a high-resolution C 1s spectrum with three characteristic peaks at 284.52, 286.02 and 287.79 eV corresponding to the C=C, C–C and N–C=N groups, respectively.[53] As displayed in Fig. 2 (C), the high resolution N 1s spectrum had two peaks at 398.53 and 399.59 eV. The peak at 398.53 was attributed to N–C, whereas that at 399.59 represents N=C bonds.[54] The occurrence of these peaks substantiated the existence of GCN in the heterojunction.

The Zn 2p spectrum shown in Fig. 2(F) had two peaks at 1044.60 and 1021.45 eV that were ascribed to Zn $2p^{1/2}$ and Zn $2p^{3/2}$ states, respectively. The Fe 2p high resolution XPS spectrum is displayed in Fig. 2(D) in which the Fe $2p^{3/2}$ peak was split into two distinct peaks. The peak centered at 709.7 eV corresponds to Fe^{3+} ions at octahedral sites, while that at 713.1 eV is assigned to Fe^{3+} in tetrahedral sites. Additionally, the presence of Fe^{3+} in octahedral sites was revealed from the Fe $2p^{1/2}$ peak positioned at 724.57 eV. The presence of Fe^{3+} in tetrahedral sites confirmed the cation exchange between the tetrahedral and octahedral sites in the lattice structure of ZFO in GCN/O_v–ZFO2. However, in the case of pristine ZFO [Fig. S2(A)], the high resolution Fe $2p^{3/2}$ peak remains intact and could not be deconvoluted, indicating the absence of Fe^{3+} ions in the tetrahedral sites. Thus, the possibility of exchange of cations has been denied in the case of pristine ZFO. The high temperature treatment applied during the fabrication of GCN/O_v–ZFO2 triggers the exchange of cations that led to the formation of vacancies in the ZFO crystal lattice.[55] This result was in good agreement with that observed in the XRD studies. A deconvoluted high-resolution O 1s XPS spectrum with three prominent peaks centered at 530.01, 531.47, and 532.7 eV is shown in Fig. 2(E). These peaks were referred to the metal bonded oxygen (Fe–O), oxygen defect sites with lower co-ordination, and hydroxyl groups resulting from the surface absorbed water molecules, respectively.[56] Fig. S2(B) compares the XPS O1s spectra of pristine ZFO and GCN/O_v–ZFO2. In the case of pristine ZFO, only two peaks appeared at 529.19 and 530.6 eV that referred to the metal bonded oxygen (Fe–O) and the surface absorbed hydroxyl groups. The third peak related to the presence of oxygen vacancies was missing in pristine ZFO. This proves the formation of an oxygen vacancy in ZFO due to the second heat treatment. Furthermore, the oxygen vacancy content in GCN/O_v–ZFO2 is calculated to be 21.6% according to the peak area distribution calculation carried out using CasaXPS software. The appearance of Zn 2p, Fe 2p and O 1s states in GCN/O_v–ZFO2 provides evidence in support of the existence of ZFO in GCN/O_v–ZFO2. The incorporation of vacancy-rich oxygen in GCN/O_v–ZFO2 was also corroborated from the high-resolution Fe 2p and O 1s XPS spectra. The presence of oxygen vacancies can create intermediate energy levels which can effectively reduce the band gap energy. The lowering of the band gap can extend the visible light absorption to a longer wavelength region.[57]

3.2. Morphology and microstructure

The morphology of the prepared samples has been assessed with the SEM technique. As can be seen from Fig. 3(A), pristine GCN exhibited a usual sheet like structure with layer formation. The sheets seem to be wrinkled and porous due to the release of ammonia gas from DCDA during the thermal condensation process. Interestingly, the pristine ZFO samples shown in Fig. 3(B) demonstrated a 2D nano-sheet morphology. Triethanolamine (TEA) influences the formation of $ZnFe_2O_4$ nanosheets by acting both as a complexing and templating agent. The donor sites in TEA form stable complexes with Zn^{2+} and Fe^{3+}. This chelation prevents premature precipitation of metal hydroxides, allowing for controlled hydrolysis and condensation reactions.[58] With the drop-wise addition of KOH, the TEA–metal complex is gradually disrupted with a slow release of TEA into the reaction system. This TEA framework then acts as a template for the nucleation of hydroxides of Zn^{2+} and Fe^{3+}. TEA has a distorted tetrahedral geometry with three flexible ethyl alcohol arms and one tertiary amine center. The nonplanar, flexible structure of TEA allows it to act as a powerful soft template which creates distinct conditions that favor lateral expansion and layered assembly. Each ethyl alcohol arm contains a hydroxyl group that can donate electron pairs to metal ions, enabling metal centers and TEA bonding, where TEA wraps around the metal centers (Zn^{2+} and Fe^{3+}). The bulky ethyl alcohol groups in TEA introduce steric hindrance, which can inhibit growth of the nano material along the upward direction. This favours lateral expansion, encouraging the formation of sheets or a plate-like morphology. On subsequent thermal treatment at 550 °C for 5 hours, TEA is completely decomposed leaving behind $ZnFe_2O_4$ with a 2D morphology. Fig. 3(C) demonstrates the SEM micro-graph of GCN/O_v–ZFO2, from which the robust contact between GCN 2D frameworks and ZFO nano-sheets in the 2D–2D heterojunction can be easily verified. The elemental colour mapping of the composites has been analyzed and is shown in Fig. 3(D)–(I). The mapping images suggested the homogenous distribution of C, N, Fe, O and Zn elements over the GCN/O_v–ZFO2 surface.

To gain further insight into the characteristics of the prepared heterojunction, TEM and HRTEM analyses of GCN/O_v–ZFO2 were carried out. The dark patches in the TEM image [Fig. 4(A)] were identified as ZFO nanosheets and the transparent areas with a loose-fold structure were designated as layered g-C_3N_4. As can be seen, the thick and dense ZFO nano-sheets are intimately covered on the rough, porous and wrinkled surface of g-C_3N_4. To ascertain the robust contact between ZFO and GCN, the magnified image of the heterojunction was obtained and presented in Fig. 4(B). By carefully examining the image, a distinct overlapped region between ZFO and GCN was identified. Thus, by combining the results from SEM and TEM analyses, we can conclude that GCN nanosheets are adhered strongly to the nanosheets of ZFO to form a sheet-on-sheet/layer-on-layer like 2D–2D arrangement. HRTEM

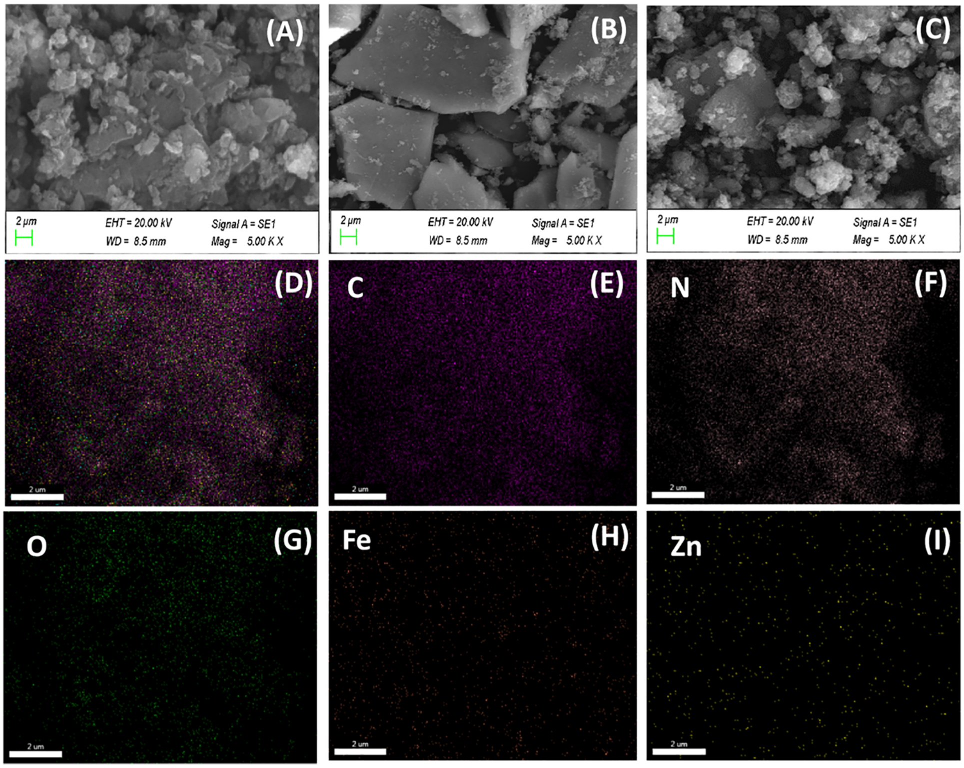

Fig. 3 SEM images of (A) GCN, (B) ZFO, (C) GCN/O_v–ZFO2 and elemental the colour mapping image of (D) GCN/O_v–ZFO2 showing the homogeneous distribution of (E) carbon, (F) nitrogen, (G) oxygen, (H) iron and (I) zinc.

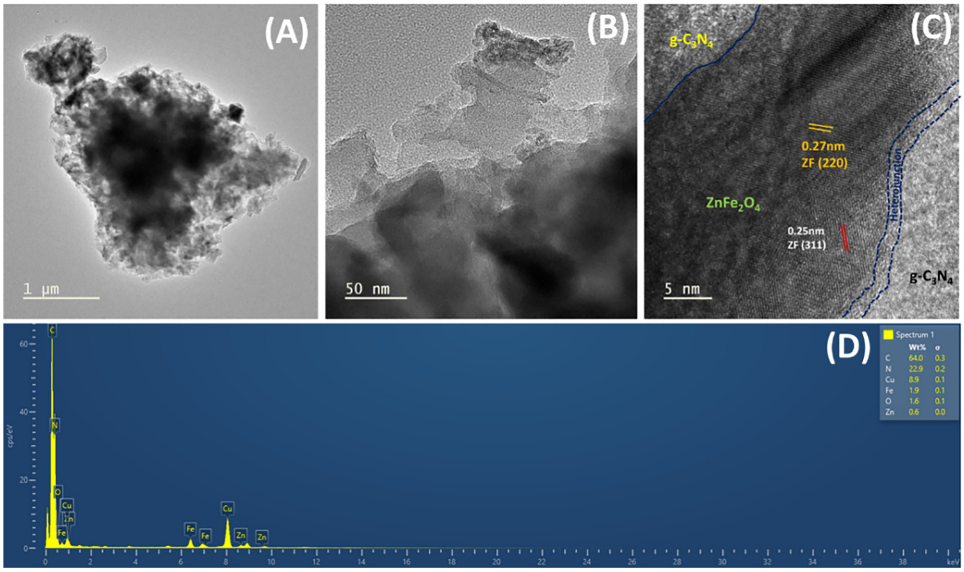

Fig. 4 TEM micro-graph at different resolutions (A) and (B), respective HRTEM image (C) and EDX spectrum (D) of GCN/O_v–ZFO2.

analysis of GCN/O_v–ZFO2 was carried out to affirm the construction of a proper heterojunction between ZFO and GCN. As shown in Fig. 4(C), two different types of patterns have been observed in the lattice arrangement of GCN/O_v–ZFO2. Both of these were identified with *d*-spacing values of 0.25 nm and 0.27 nm that belong to the (311) and (220) planes of cubic ZFO.[53] The less-prominent area in the image has been identified as amorphous GCN since no lattice patterns were observed in this region. The hetero-interface between GCN and ZFO is very much distinguishable and has been highlighted in blue colour. Additionally, the EDX spectrum of the composite shown in Fig. 4(D) suggests the presence of C, N, O, Fe, and Zn elements in the composite. The appearance of Cu peaks in EDX spectra originates from the supporting copper mesh. These results confirmed the formation of a robust 2D–2D heterojunction between ZFO and GCN.

The low-temperature N_2 adsorption–desorption isotherms of the prepared GCN, ZFO and GCN/O_v–ZFO2 are shown in Fig. S3(A), (B) and Fig. 5(A), respectively. All of the samples demonstrated a type IV isotherm with a H3 hysteresis loop, suggesting mesoporous nature. The BET analysis revealed that the specific surface areas of GCN and ZFO [Fig. S2(A) and (B)] were 32.21 and 19.24 m^2 g^{-1}. Pure GCN shows a larger surface area than ZFO due to its wrinkled and porous structure according to SEM analysis results. However, when we couple GCN with ZFO to construct a GCN/O_v–ZFO2 2D–2D heterostructure the specific surface area significantly increases to 47.86 m^2 g^{-1}. The larger specific surface area observed for GCN/O_v–ZFO2 may be ascribed to the extended sheet-on-sheet arrangement between 2D nanosheets of ZFO and GCN, as revealed from TEM images. The heterojunction construction could possibly accumulate a larger amount of surface active sites that is beneficial for achieving augmented photocatalytic activity.[59] The BJH pore size distribution curve displayed in Fig. 5(B) suggests an average pore diameter of 4.88 nm with a pore volume of 0.0805 cc g^{-1}, which further confirmed the mesoporous architecture of the GCN/O_v–ZFO2 heterojunction. Elevated specific surface area can provide a sufficient amount

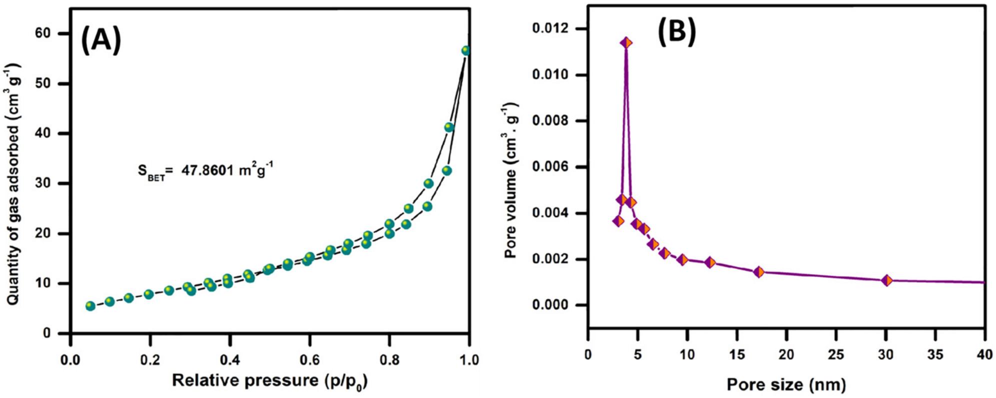

Fig. 5 (A) BET specific surface area and (B) BJH pore size distribution curve of GCN/O_v–ZFO2.

of surface active sites that help in the faster surface redox reactions, whereas the mesopores facilitated the adsorption of reactants over GCN/O$_v$–ZFO2.[60] As a whole, the observed textural properties eventually contribute towards elevated photocatalytic activity.

3.3. Optical properties

Fig. 6(A) depicts the UV-visible diffusive reflectance spectra of GCN, ZFO, and GCN/O$_v$–ZFO2 photocatalysts. From the diagram, the absorption edge of pristine GCN was found to be around 458 nm. Meanwhile, ZFO demonstrated a longer light absorption window, indicating that the narrower band gap endowed the material with upscale visible light activity. The addition of ZFO to GCN leads to a bathochromic shift in the light absorption of GCN/O$_v$–ZFO2 from 458 to 535 nm. The high visible light activity of ZFO and sturdy interaction of energy bands between ZFO and GCN in the GCN/O$_v$–ZFO2 heterojunction are responsible for the observed phenomenon.[61]

Additionally, the GCN/O$_v$–ZFO2 composite shows an Urbach tail between the wavelengths of 450 and 700 nm. Due to the presence of structural imperfections, localized energy states were formed, giving rise to this feature. The oxygen vacancies induce a defect energy level beneath the conduction band, as mentioned in the literature.[62] The appearance of these mid-gap energy levels makes it possible for photons with energies below the semiconductor's optical gap to be absorbed. This phenomenon is known as enhanced sub-bandgap absorption.[63] Hence, the UV-visible DRS spectra suggested that the formation of oxygen vacancies and robust heterojunction construction have a synergistic effect on the extended visible light absorption ability of GCN/O$_v$–ZFO2. Higher visible light absorption ensures the formation of a sufficient amount of photo-induced charge carriers for upgraded photocatalytic performance.

The Kubelka–Munk equation given in eqn 6 was employed to estimate the band gap (E_g) values of pristine ZFO and GCN.

$$(\alpha h\nu)^n = A(h\nu - E_g) \tag{6}$$

where α, h, ν, n and A are the absorption coefficient, Planck constant, optical frequency, electronic transition and proportionality constant, respectively. The band gap value (E_g) of GCN was determined to be 2.80 eV by extrapolating the tangent from the Kubelka–Munk plots to the X-axis in Fig. 6(B). Similarly, the bandgap energy of ZFO is obtained to be 1.92 eV [Fig. 6(C)]. The band potentials for the CBM and VBM of GCN and ZFO were calculated using eqn (7) and (8).

$$E_{VB} = X - E^e + 0.5E_g \tag{7}$$

$$E_{CB} = E_{VB} - E_g \tag{8}$$

Here, E_{VB} is the VBM (valence band maxima) potential and E_{CB} is the CBM (conduction band minima) potential. X is calculated by taking the geometric mean of the absolute electronegativity of the constituent atoms. The energy of free electrons on the hydrogen scale is referred to as E^e (about 4.5 V), and the band gap energy of the semiconductor is denoted as E_g. By putting the respective values of X, E^e and E_g, in eqn (7), the VB potentials of GCN and ZFO were determined to be +1.63 and

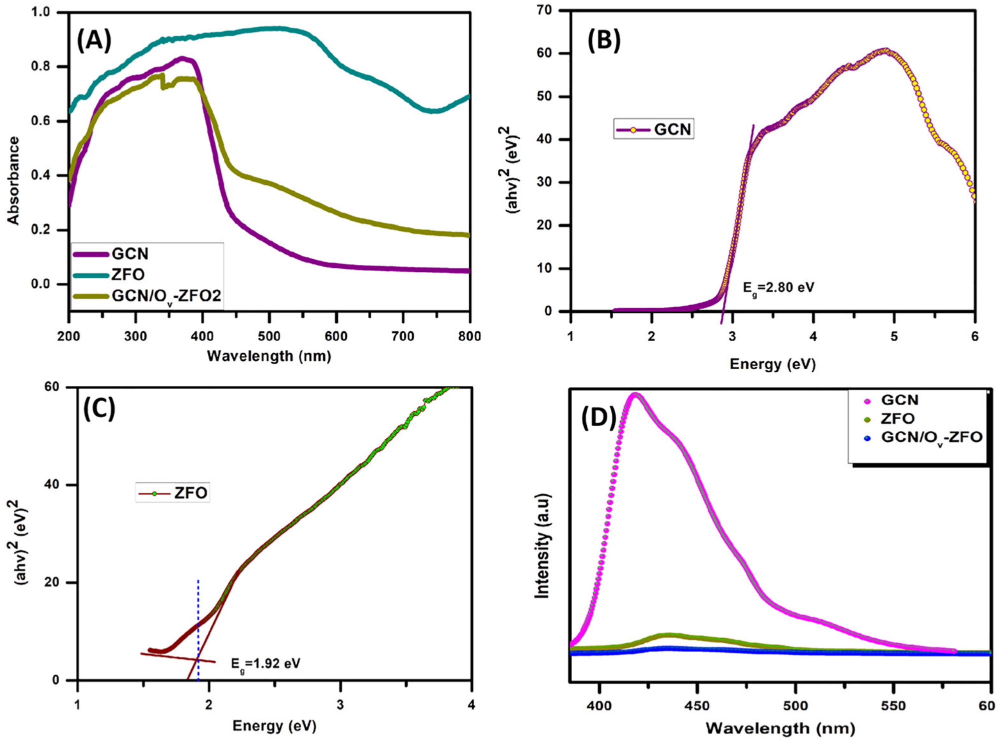

Fig. 6 (A) UV-Visible DRS spectra of GCN, ZFO and GCN/O$_v$–ZFO2, estimated band gaps of (B) GCN and (C) ZFO, and (D) PL emission spectrum of ZFO and GCN/O$_v$–ZFO2.

2.31 V, respectively. The corresponding CB potentials were calculated to be −1.17 and 0.39 V from eqn (8) using the values of E_{VB} and E_g.

To obtain the required evidence in support of prolonged charge carrier lifetime, photoluminescence (PL) analysis of the produced catalysts was carried out. While a lower PL intensity shows a longer lifespan of the photoinduced charge carriers, a higher PL response often suggests a faster rate of charge carrier recombination.[64] As shown in Fig. 6(D), the PL graph of pure GCN shows a very large curvature with high intensity. This suggests that GCN experiences increased charge recombination because of poor charge transport and narrow conduction pathways. To reduce charge recombination and improve efficiency we have coupled O-deficient ZFO with GCN to construct a 2D–2D Z-scheme heterojunction. As can be interpreted from the figure, the steady PL intensity of the GCN/O_v–ZFO2 heterojunction is lower than those of bare ZFO and GCN, implying the lowest charge transfer resistance at the interface.

3.4. Electrochemical studies

To elucidate the charge separation and transfer ability of the prepared catalysts, linear sweep voltammetry (LSV) and electrochemical impedance study (EIS) were carried out. LSV curves are presented in Fig. 7(A) to study the current density and charge transfer behaviour of the prepared materials. Among all the prepared catalysts, the GCN/O_v–ZFO2 heterojunction exhibited a maximum current density of 0.53 mA cm^{-2} which is 2.1 and 1.26 times higher than those of GCN and ZFO, respectively. The higher current density over GCN/O_v–ZFO2 indicated the availability of an ample amount of free charge concentration, resulting from the augmented separation of photo generated charge carriers.[65] These observations were in line with the conclusions derived from PL analysis. To verify the results obtained from the LSV technique, the resistance associated with charge migration at the electrode–electrolyte interface was measured using the EIS technique. The arc radius of the curves in the nyquist plot presented in Fig. 7(B) demonstrated the charge transfer resistance at the interface. A lower arc radius suggests minimum charge transfer resistance, which is a direct indicator of enhanced charge migration efficiency.[66] From the figure, GCN/O_v–ZFO2 showed the minimum arc radius in comparison to ZFO and GCN. This suggested upgraded charge transfer kinetics in the GCN/O_v–ZFO2 heterojunction owing to lower resistance and higher separation of electron–hole pairs, as evident previously from the LSV study. These results substantially demonstrated higher charge transfer and separation efficiency of GCN/O_v–ZFO2 due to the construction of a 2D–2D hetero-interface between GCN and O_v-ZFO.

Mott–Schottky (MS) analysis of GCN and ZFO was carried out at different frequencies to manifest their electronic band structures. As depicted in Fig. 7(C) and (D), the positive slopes of curves imply that these two samples are n-type semiconductors. The flat band potentials of GCN and ZFO were determined to be −1.71 and −0.22 V (*vs.* Ag/AgCl, pH = 7), respectively, which are equivalent to −1.12 and 0.38 V (*vs.* RHE), respectively, calculated by applying the Nernst equation.

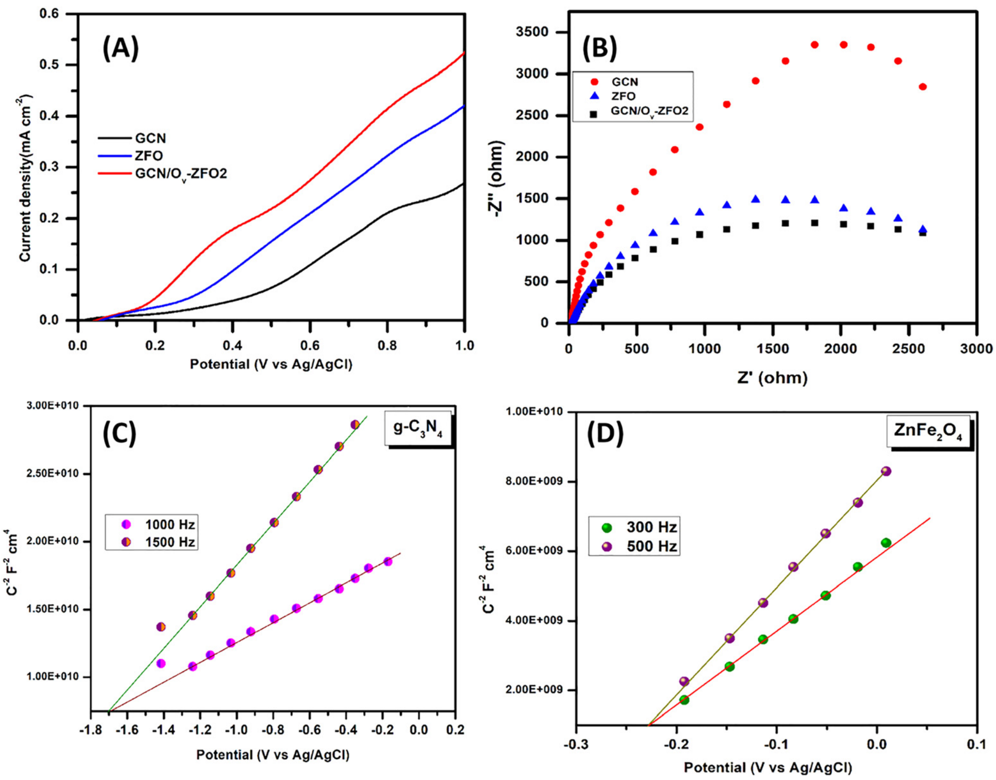

Fig. 7 (A) LSV and (B) EIS plots of GCN, ZFO and GCN/O_v–ZFO2, and MS plots of (C) GCN and (D) ZFO.

$$E_{\mathrm{RHE}} = E_{\mathrm{Ag/AgCl}} - 0.0591(-\text{pH of the electrolyte}) + 0.198 \tag{9}$$

The n-type semiconductor's Fermi energy levels (E_f) lie very close to the CB.[67] Thus the CBs of GCN and ZFO were calculated to be positioned at −1.12 V and 0.38 V (*vs.* RHE), respectively. The VB levels of the pristine materials were calculated by using eqn (8) to be 1.68 and 2.30 V (*vs.* RHE) for GCN and ZFO, respectively. These values are almost similar to the band position values obtained from the electronegativity calculations presented in Section 3.3.

3.5. Photocatalytic performance

3.5.1. MO detoxification. For the degradation of MO, an appropriate amount of catalyst was introduced to a 15 mg L^{-1} MO solution and left in the dark for 30 minutes prior to photodegradation. The photocatalytic activity of various photocatalysts toward MO breakdown is displayed in Fig. 8(A). From the figure, it was evident that, the adsorption of MO achieves equilibrium after 30 minutes under dark conditions. The GCN, ZFO, and GCN/O_v–ZFO samples show less than 10% adsorption after achieving adsorption–desorption equilibrium, indicating that most of the MO are eliminated through the photocatalytic degradation process. After 60 minutes of reaction, pure GCN and ZFO had photocatalytic degradation rates of 53.12% and 26.38%, respectively. With the increase in the GCN content in the heterojunction, the photocatalytic activity enhanced drastically as GCN/O_v–ZFO1 and GCN/O_v–ZFO2 exhibited 79.41% and 99.54% of MO degradation, respectively. This enhancement in activity can be attributed to the effective charge carrier transfer and separation at the elongated 2D–2D hetero-interface of the GCN/O_v–ZFO nanocomposites. Furthermore, the thermal treatment-induced oxygen vacancies act as trapping sites for charge carriers as well as enhance the visible light absorption range. However, a further increase in the GCN content resulted in a diminished activity of 65.6% for GCN/O_v–ZFO3. The excessive loading of GCN over the ZFO surface reduces the active sites and obstructs the charge migration that resulted in lower activity.[68,69] This finding demonstrated that the photocatalytic activity of the GCN/O_v–ZFO heterojunction can be increased following the deposition of the appropriate amount of GCN. The photodegradation kinetics of MO over different catalysts has been studied and the results are given in Fig. 8(B). The pseudo-first-order rate constants (k) for MO photodegradation over GCN, ZFO, GCN/O_v–ZFO1, GCN/O_v–ZFO2, and GCN/O_v–ZFO3 nanocomposites were calculated to be 0.012, 0.005, 0.032, 0.047, and 0.021 min^{-1}, respectively. GCN/O_v–ZFO2 exhibited the highest rate constant value which is 4 times and 9.4 times greater than that of GCN and ZFO, respectively.

3.5.2. Photocatalytic hydrogen generation. Photocatalytic H_2 production over GCN, ZFO and GCN/O_v–ZFO composite catalysts was carried out by using methanol as a sacrificial agent. Fig. 8(C) shows the H_2 production activity of the

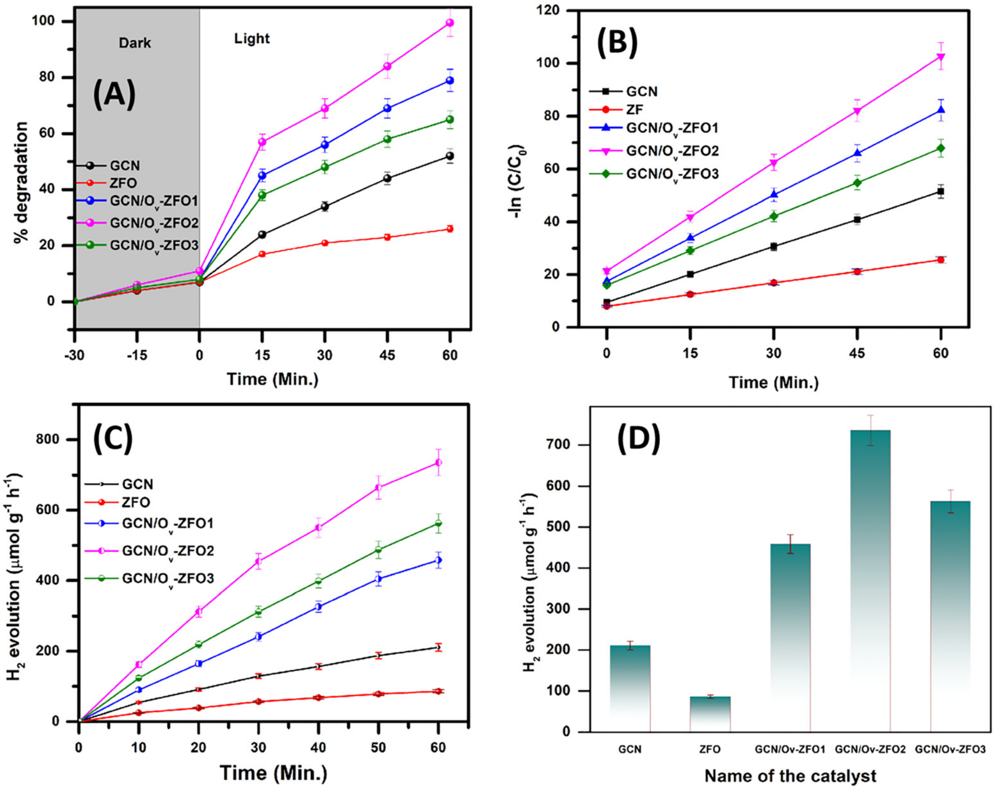

Fig. 8 (A) Photocatalytic MO degradation efficiencies, (B) linearly fitted kinetic plots, (C) photocatalytic H_2 evolution performance and (D) H_2 evolution rates of GCN, ZFO, GCN/O_v–ZFO1, GCN/O_v–ZFO2, and GCN/O_v–ZFO3 catalysts.

as-prepared samples under visible light illumination for 60 minutes. The photocatalytic H_2 generation rate increases linearly with an increase in time, which indicates the favourable surface reaction kinetics for the prepared catalysts. GCN/O_v–ZFO2 exhibited a maximum photocatalytic H_2 evolution rate of 735.4 μmol g^{-1} h^{-1} which is 3.6 and 8.5 times greater than those of GCN (201.7 μmol g^{-1} h^{-1}) and ZFO (86 μmol $g^{-1}h^{-1}$), respectively. As illustrated in Fig. 8(D), the GCN/O_v–ZFO2 nanocomposite exhibits the highest H_2 evolution rate among all the prepared samples. The ameliorated activity of GCN/O_v–ZFO2 could be attributed to several factors: (1) the presence of oxygen vacancies can intensify the surface reactivity of the GCN/O_v–ZFO2, making it more efficient for adsorption and activation of the target molecule (water), (2) the 2D–2D heterojunction construction promotes the effective separation and transfer of the photogenerated charge carriers at the extended interface that resulted in diminished recombination, and (3) a broader light absorption window of GCN/O_v–ZFO2 promotes photon absorption to a great extent. All these factors cumulatively contributed toward higher visible light active photocatalytic hydrogen production ability of the GCN/O_v–ZFO2 nanocomposite. The MO degradation efficiency and H_2 production rate obtained in the present work were compared with those reported in the literature in Tables 1 and 2, respectively.[70–82]

3.5.3. Reusability and stability.

The recyclability of GCN/O_v–ZFO2 was evaluated by photocatalytic MO degradation and H_2 production for five consecutive cycles. As shown in Fig. 9(A), the maximum MO degradation ability of GCN/O_v–ZFO2 for the mentioned five cycles has been 99.54, 92.67, 86.32 81.6, and 78.2%, respectively. Similarly, the photocatalytic H_2 evolution rate was measured to be 735.4, 712.3, 694.1, 678.3, and 652.9 μmol g^{-1} h^{-1} for the five respective cycles [Fig. 9(B)]. The decreasing trend in photocatalytic activity with every cycle signifies the loss of catalytic active sites of the heterojunction photocatalyst owing to the continued interaction with the MO and water molecules.[83,84] The high efficiency of MO degradation and the H_2 production rate of GCN/O_v–ZFO2 after the fifth use demonstrated its efficient reusability. Furthermore, XRD analyses of the fresh and used catalysts were carried out to elucidate the phase transformation of GCN/O_v–ZFO2. As shown in Fig. 9(C), similar XRD patterns for the fresh and spent catalyst were observed, indicating no significant changes in the crystallinity and phase structure of GCN/O_v–ZFO2 after five cycles of MO degradation. The structural stability of GCN/O_v–ZFO2 was assessed by examining the FTIR spectra before and after photocatalytic MO degradation. As shown in Fig. 9(D), nearly all the major peaks related to GCN and ZFO have retained their positions in the FTIR spectra of the spent catalyst. However, changes were observed for the peaks related to the OH stretching mode. In the case of the used catalyst, a broad band with higher intensity was observed which can be assigned to the absorbed water molecules over the catalyst resulting from the degradation of the MO dye.[85] This evidence suggested the retention of structural stability of GCN/O_v–ZFO2 after five cycles of continuous use. Furthermore, no peak related to MO was observed in the FTIR spectra, suggesting its complete mineralization.[86]

3.5.4. Photocatalytic reaction mechanism.

In order to figure out the probable reaction mechanism for MO photodegradation, scavenging experiments were carried out. Triethanolamine (TEA), *p*-benzoquinone (BQ), and isopropanol (IPA) were used as scavengers in this experiment to effectively quench the activity of h^+, $^{\bullet}O_2^-$, and $^{\bullet}OH$ radicals, respectively.[87] As shown in Fig. 10(A), the photodegradation efficiencies of MO over GCN/O_v–ZFO-2 are 44.5% with BQ, 51.23% with IPA and 68.2% with TEA. This suggests that the major reactive species for MO photodegradation over GCN/O_v–ZFO2 are $^{\bullet}O_2^-$ and $^{\bullet}OH$ radicals. Meanwhile, the quenching of h^+ has a moderate effect on the efficiency. To confirm the charge transfer dynamics between the pristine ZFO and GCN in the heterojunction, the C 1s and N 1s XPS spectra of GCN and GCN/O_v–ZFO2 are compared in Fig. 10(B) and (C), respectively. It was observed that the XPS peaks in both the C 1s and N 1s spectra have been shifted to lower binding energies in GCN/O_v–ZFO2 as compared to pristine GCN. This observation suggested the accumulation of electrons over the GCN surface when in contact with ZFO in the heterojunction.[88] In contrast, a comparison of the O1s, Fe 2p and Zn 2p XPS spectra of ZFO and GCN/O_v–ZFO2, illustrated in Fig. 10(D), (E) and (F), respectively, exhibited a different trend. These peaks have shifted to a higher binding energy values in the case of the heterojunction

Table 1 Comparison of the photocatalytic MO degradation ability of the prepared GCN/O_v–ZFO2 photocatalyst with that of similar heterojunction systems

Catalyst	Light source	Catalyst dose (g L^{-1})	Time (Min.)	MO conc.	(%) MO removed	K (min^{-1})	Ref.
K doped $g-C_3N_4/ZnIn_2S_4$ Z scheme	5 W LED	0.25	60	10 ppm	97.6	0.07	70
$CuS/g-C_3N_4$	300 W Xe lamp	0.5	60	10 ppm	53.9	0.008	71
$ZnIn_2S_4/g-C_3N_4$	500 W Xe lamp	0.4	120	10 ppm	95.31	_	72
$CoFe_2O_4/g-C_3N_4$	300 W Xe lamp	1	240	10^{-5} M	98	_	73
$Zn_3In_2S_6$/F doped $g-C_3N_4$	300 W Xe lamp	0.4	60	10 ppm	99	0.07	74
$TiO_2/g-C_3N_4$	300 W Xe lamp	1	180	10 ppm	55	0.004	75
$ZnO/g-C_3N_4$ Z-scheme	150 W Xe lamp	1	360	10^{-5} M	88	0.0041	76
$g-C_3N_4/O_v-WO_3$	Xe lamp	0.5	75	10 ppm	91.8	0.0299	77
$g-C_3N_4/WO_3$ Z-scheme	300 W Xe lamp	0.3	100	10 ppm	49.6	_	78
$ZnFe_2O_4/AgI$	70 W Metal hallide lamp	1	180	10 ppm	89.3	_	79
$O_v-ZnFe_2O_4/g-C_3N_4$ 2D–2D Z-scheme	250 W Xe lamp	0.4	60	15 ppm	99.4	0.047	This work

Table 2 Comparison of photocatalytic H_2 generation efficiency of GCN/O_v–ZFO2 with that of recently reported literature

Catalyst	Light source	Catalyst dose	Time (Min.)	Scavenger	H_2 evolution rate (μmol g^{-1} h^1)	Ref.
$ZnIn_2S_4$/g-C_3N_4	300 W Xe lamp	0.4 g L^{-1}	180	TEOA	510	72
$CoFe_2O_4$/g-C_3N_4	500 W Hg Lamp	8.3 g L^{-1}	60	Methanol	0	73
TiO_2/g-C_3N_4 (Pt)	300 W Xe lamp	1 g L^{-1}	180	TEOA	1058	75
ZnO/g-C_3N_4 Z-scheme	150 W Xe lamp	1 g L^{-1}	360	–	0	76
$ZnFe_2O_4$/g-C_3N_4 (Pt)	Sunlight	3 mg	240	Methanol	1752	60
Ni-$ZnFe_2O_4$/g-C_3N_4	300 W Xe lamp	10 mg	240	TEOA	88.25	80
$CuNiSnS_4$/g-C_3N_4 S-scheme	Sunlight 65,000 lux	0.1 g L^{-1}	240	Methanol	4.6	81
ZnO/$ZnFe_2O_4$	250 W Xe lamp	1 mg mL^{-1}	300	Methanol	530	82
O_v-$ZnFe_2O_4$/g-C_3N_4 2D–2D Z-scheme	250 W Xe lamp	0.4 g L^{-1}	60	Methanol	735.4	This work

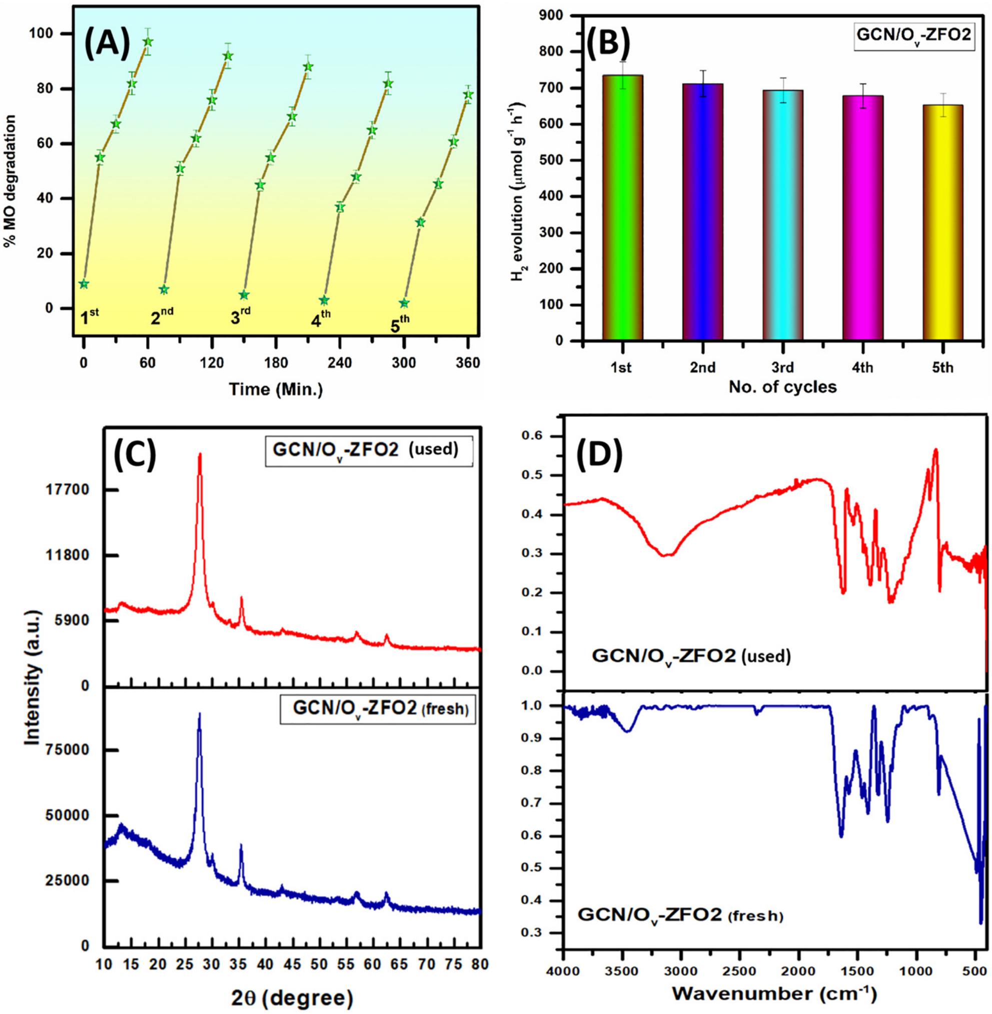

Fig. 9 Photocatalytic (A) MO degradation curves and (B) rate of H_2 evolution in the reusability test of the GCN/O_v–ZFO2 catalyst for five consecutive cycles, and comparison of (C) XRD and (D) FTIR spectrum of fresh and used GCN/O_v–ZFO2 catalysts.

composite, suggesting a decline in electron density over the ZFO surface in GCN/O_v–ZFO2.

Based on scavenger studies, XPS analysis and band potential calculations, a potential reaction mechanism for photocatalytic MO degradation and hydrogen evolution over GCN/O_v–ZFO2 nanocomposites is proposed. As evident from the UV-Visible DRS spectral analysis, the light absorption range of GCN/O_v–ZFO2 is extended up to 535 nm owing to the presence of oxygen vacancies as well as highly visible light active ZFO. The oxygen vacancies create a mid-gap energy level as illustrated by the appearance of the Urbach tail in the extended region (450–700 nm). Due to the structural imperfections in the form of oxygen vacancies, localized mid-gap energy states were formed that can absorb photons with lower energy, giving rise to augmented visible light absorption. This process enhances photon absorption capacity of GCN/O_v–ZFO2, which gives rise

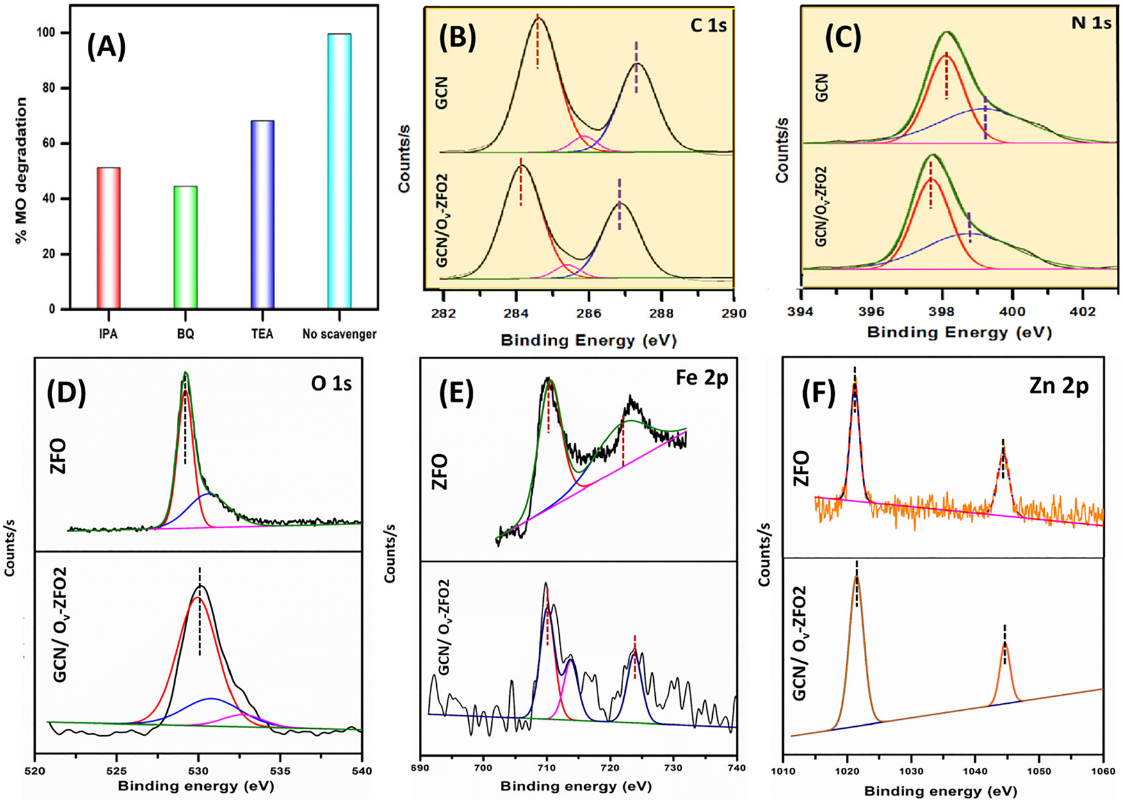

Fig. 10 (A) Scavenging experiment results for MO, comparison of high resolution (B) C 1s and (C) N 1s XPS spectra of pristine GCN and (D) O 1s, (E) Fe 2p and (F) Zn 2p spectra of pristine ZFO with that of GCN/O$_v$–ZFO2.

to production of an ample amount of electron–hole pairs, which in general contribute towards elevated photocatalytic activity.

On exposure to visible light, electrons and holes were formed at the CB and VB of both GCN and ZFO. The electrons accumulated at the CB of ZFO possess inadequate ability to undergo the oxygen reduction reaction (ORR) since its CB position (0.39 V) is more positive than that required for $^{\bullet}O_2^-$ radical generation $\left(E^0_{O_2/{}^{\bullet}O_2^-} = -0.33\ \text{V}\right)$. However, the CB of GCN (−1.17 V) is more negative than that of $E^0_{O_2/{}^{\bullet}O_2^-}$, thus the electrons in the CB of GCN preferably undergoes the ORR to produce $^{\bullet}O_2^-$ radicals. Similarly, the holes present over ZFO generate $^{\bullet}OH$ radicals through the water oxidation reaction (WOR) as the VB of ZFO is placed at a more cathodic potential (2.31 V) than the standard oxidation potential of water $\left(E^0_{H_2O/{}^{\bullet}OH} = 2.28\ \text{V}\right)$. Concurrently, the $^{\bullet}O_2^-$ and $^{\bullet}OH$ radicals along with the photoproduced holes directly oxidize MO into CO_2 and H_2O. Meanwhile, the electrons present in the CB of ZFO with weaker redox ability can migrate towards the VB of GCN to recombine with the holes owing to the Fermi energy difference between ZFO and GCN.[89] Therefore, the electrons in the CB of GCN and holes in the VB of ZFO with strong redox ability are available for photocatalytic degradation of MO as shown in eqn (10)–(13). This evidence corroborates the formation of the GCN/O$_v$–ZFO direct Z-scheme heterojunction.

$$\text{GCN/O}_v\text{–ZFO} + h\nu \rightarrow e^- + h^+ \tag{10}$$

$$O_2 + e^- \rightarrow O_2^{\bullet -} \tag{11}$$

$$H_2O + h^+ \rightarrow {}^{\bullet}OH \tag{12}$$

$$O_2^{\bullet -} + {}^{\bullet}OH + h^+ + \text{MO} \rightarrow H_2O + CO_2 \tag{13}$$

The plausible mechanism for photocatalytic hydrogen generation over GCN/O$_v$–ZFO2 proceeds through a direct Z-scheme charge transfer system as per the following steps. At first, the photo-generated holes available in the VB of ZFO with more positive potential undergo the WOR to liberate $^{\bullet}OH$ radicals as shown in eqn (12). In the second step, methanol being the hole scavenger reacts with the remaining holes accumulated in the VB of ZFO to produce formaldehyde through the generation of hydroxyl methyl radicals ($^{\bullet}CH_2OH$) as the intermediate according to eqn (14) and (15). In the subsequent steps, formaldehyde undergoes oxidation reactions with holes and $^{\bullet}OH$ radicals to produce CO_2 and H_2O as final products (eqn (14)–(18)).[90]

$$CH_3OH + h^+ \rightarrow {}^{\bullet}CH_2OH + H^+ \tag{14}$$

$$^{\bullet}CH_2OH + h^+ \rightarrow HCHO + H^+ \tag{15}$$

$$HCHO + {}^{\bullet}OH + h^+ \rightarrow HCOOH + H^+ \tag{16}$$

$$HCOOH \rightarrow HCOO^- + H^+ \tag{17}$$

$$HCOO^- + 2h^+ \rightarrow CO_2 + H^+ \tag{18}$$

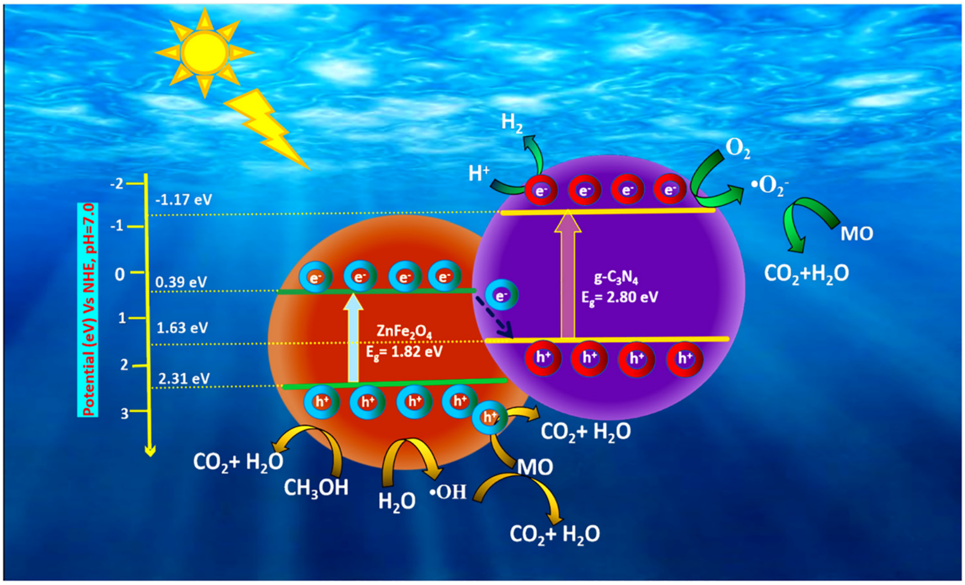

Scheme 2 Diagrammatic representation of photocatalytic H_2 production and MO degradation using the 2D–2D GCN/O_v–ZFO2 direct Z-scheme heterojunction nanocomposite.

On the other hand, electrons trapped in the CB of g-C_3N_4 being possessed with a more negative potential than that required for hydrogen reduction $\left(E^0_{H^+/H_2} = 0\,V\right)$ reduce the protons generated from the consecutive oxidation reactions to produce gaseous hydrogen (eqn (19)).

$$2H^+ + 2e^- \rightarrow H_2 \qquad (19)$$

This extensive photodegradation mechanism clarifies that the GCN/O_v–ZFO-2 nanocomposite could create a direct Z-scheme charge transfer dynamics to efficiently photo-oxidize MO dye effluents and generate gaseous hydrogen, as illustrated in Scheme 2.

4. Conclusion

A morphology-aligned 2D–2D g-C_3N_4/O_v-$ZnFe_2O_4$ direct Z-scheme heterojunction was synthesized for efficient photocatalytic degradation of MO dye and hydrogen generation. The unique 2D architecture of ZFO was resulted from the synergistic role of triethanolamine (TEA) as a complexing agent and a template. XRD analysis indicated the reduced crystallite size, increased lattice microstrain, and decreased lattice parameters in GCN/O_v–ZFO2, suggesting defect incorporation. The presence of oxygen vacancies, induced by cation disorder during high-temperature treatment, was confirmed from the XPS O 1s spectra. These vacancies serve as active sites for molecular adsorption and create mid-gap states that enhance visible-light absorption. Electron microscopy techniques (SEM, TEM, and HRTEM) confirmed the formation of a robust 2D–2D heterojunction with tightly bonded nanosheets. PL spectra demonstrated enhanced spatial charge separation and reduced recombination, reinforcing the charge transfer efficiency of the 2D/2D heterojunction. The combined results of radical trapping experiments, XPS analysis and band potential calculations provided robust evidence for the optimized carrier separation while preserving redox potential. The combined effects of the 2D–2D heterojunction, oxygen vacancies, and Z-scheme charge transfer dynamics significantly augmented photocatalytic activity. GCN/O_v–ZFO_2 achieved an impressive MO degradation rate of 99.54%, outperforming pristine ZFO (26.38%) and GCN (53.12%). Moreover, it retained its catalytic efficiency across five successive cycles. The photocatalytic hydrogen evolution rate of GCN/O_v–ZFO_2 reached 735.4 μmol g^{-1} h^{-1}, surpassing those of GCN and ZFO by factors of 3.6 and 8.5, respectively. These results position 2D–2D direct Z-scheme GCN/O_v–ZFO heterojunctions as promising candidates for diverse photocatalytic applications.

Author contributions

Subhasish Mishra: investigation, data curation, and writing (original draft); Rashmi Acharya: conceptualization, methodology, supervision, and writing (review and editing); Bhagat Lal Tudu and Kali Sanjay: methodology, validation and formal analysis; and Nimai Mishra: formal analysis.

Conflicts of interest

There are no conflicts to declare.

Data availability

All data generated or analyzed in this study are included in the main article and the supplementary information (SI). Supplementary information is available. See DOI: **https://doi.org/10.1039/d5ma00533g**.

Acknowledgements

SM and RA gratefully acknowledge the management of Siksha 'O' Anusandhan (Deemed to be University), Bhubaneswar, Odisha, India, for their constant support in completing this study.

References

1 A. Mehtab and T. Ahmad, unveiling the bifunctional photo/electrocatalytic activity of in situ grown CdSe QDs on g-C_3N_4 nanosheet Z-Scheme heterostructures for efficient hydrogen generation, *ACS Catal.*, 2024, **14**, 691.

2 A. Jamma, B. Jaksani, C. S. Vennapoosa, S. Gonuguntla, S. Sk and M. Ahmadipour, M. A. B., I. Mondal, and U. Pal, Defect-rich UiO-66@g-C_3N_4/Ni frameworks as efficient water splitting photocatalysts, *Mater. Adv.*, 2024, **5**, 2785–2796.

3 M. Uzzaman, M. H. Suhag, H. Katsumata, I. Tateishi, M. Furukawa and S. Kaneco, A graphitic carbon nitride photocatalyst with a benzene-ring-modified isotype heterojunction for visible-light-driven hydrogen production, *Catal. Sci. Technol.*, 2024, **14**, 267–278.

4 S. Hu, M. Gao, J. Huang, H. Wang, Q. Wang, W. Yang, Z. Sun, X. Zheng and H. Jiang, Introducing Hydrogen-Bonding Microenvironment in Close Proximity to Single-Atom Sites for Boosting Photocatalytic Hydrogen Production, *J. Am. Chem. Soc.*, 2024, **146**(29), 20391–20400.

5 Y. Quan, J. Li, X. Li, R. Chen, Y. Zhang, J. Huang, J. Hu and Y. Lai, Molten salt-assisted synthesis of carbon nitride with defective sites as visible-light photocatalyst for highly efficient hydrogen evolution, *Appl. Catal., B*, 2025, **362**, 124711.

6 A. A. Levikhin and A. A. Boryaev, High-temperature reactor for hydrogen production by partial oxidation of hydrocarbons, *Int. J. Hydrogen Energy*, 2023, **48**, 28187–28204.

7 M. Younas, S. Shafique, A. Hafeez, F. Javed and F. Rehman, An overview of hydrogen production: current status, potential, and challenges, *Fuel*, 2022, **316**, 123317.

8 S. Mishra, R. Acharya and K. Parida, Spinel-ferrite-decorated graphene-based nanocomposites for enhanced photocatalytic detoxification of organic dyes in aqueous medium: a review, *Water*, 2023, **15**, 81.

9 Z. Wang, H. Wang, P. Shi, J. Qiu, R. Guo, J. You and H. Zhang, Hybrid organic frameworks: Synthesis strategies and applications in photocatalytic wastewater treatment - A review, *Chemosphere*, 2024, **350**, 141143.

10 V. Q. Hieu, T. K. Phung, T. Nguyen, A. Khan, V. D. Doan, V. A. Tran and V. T. Le, Photocatalytic degradation of methyl orange dye by Ti_3C_2–TiO_2 heterojunction under solar light, *Chemosphere*, 2021, **276**, 130154.

11 A. Chen, Y. Xie, R. Lu, J. Luo, T. Shang, Y. Xu, D. Jiang and Q. Zhan, Z-scheme Bi_2SiO_5/Ni-doped $Ag_6Si_2O_7$ heterojunction with remarkable photocatalytic performance for MO degradation with enhanced light absorption ability: Adjustment of electron transfer path and energy band structure, *Appl. Surf. Sci.*, 2024, **642**, 158.

12 K. G. Pavithra, P. S. Kumar, V. J. aikumar and P. S. Rajan, Removal of colorants from wastewater: a review on sources and treatment strategies, *J. Ind. Eng. Chem.*, 2019, **75**, 1–19.

13 S. Kumari, K. Sharma, S. Korpal, J. Dalal, A. Kumar, Supreet, S. Kumar and S. Duhan, A comprehensive study on photocatalysis: materials and applications, *Cryst. Eng. Comm.*, 2024, **26**, 4886–4915.

14 P. Kumar, S. Kaushal, S. Kumar, J. Dalal, K. M. Batoo and D. S. Ahlawat, Recent advancements in pure and doped zinc oxide nanostructures for UV photodetectors application, *Phys. B: Cond. Matter*, 2025, **707**, 417177.

15 P. Vijayarengan, S. C. Panchangam, A. Stephen, G. Bernatsha, G. K. Murali, S. S. Loka, S. K. Manoharan, V. Vemula, R. R. Karri and G. Ravindran, Highly efficient visible light active iron oxide-based photocatalysts for both hydrogen production and dye degradation, *Sci. Rep.*, 2024, **14**, 18299.

16 A. A. P. Khan, A. Sudhaik, P. Raizada, A. Khan and M. A. Rub, AgI coupled SiO_2@$CuFe_2O_4$ novel photocatalytic nanomaterial for photo-degradation of organic dyes, *Catal. Commun.*, 2023, **179**, 106685.

17 P. Dhull, A. Sudhaik, P. Raizada, S. Thakur, V.-H. Nguyen, Q. V. Le, N. Kumar, A. A. P. Khan, H. M. Marwani, R. Selvasembian and P. Singh, An overview on ZnO-based sonophotocatalytic mitigation of aqueous phase pollutants, *Chemosphere*, 2023, **333**, 138873.

18 M. A. Ahmed, S. A. Mahmoud and A. A. Mohamed, Unveiling the photocatalytic potential of graphitic carbon nitride (g-C_3N_4): a state-of-the-art review, *RSC Adv.*, 2024, **14**, 25629–25662.

19 H. M. Solayman, A. A. Aziz, N. Y. Yahya, K. H. Leong, L. C. Sim, M. K. Hossain, M. B. Khan and K. Zoh, CQDs embed g-C_3N_4 photocatalyst in dye removal and hydrogen evolution: An insight review, *J. Water. Proc. Eng.*, 2024, **57**, 104645.

20 R. Acharya and K. Parida, A review on TiO_2/g-C_3N_4 visible-light- responsive photocatalysts for sustainable energy generation and environmental remediation, *J. Environ. Chem. Eng.*, 2020, **8**, 103896.

21 H. Hou, G. Shaob and W. Yang, Recent advances in g-C_3N_4-based photocatalysts incorporated by MXenes and their derivatives, *J. Mater. Chem. A*, 2021, **9**, 13722–13745.

22 R. Acharya, S. Pati and K. Parida, A review on visible light driven spinel ferrite-g-C_3N_4 photocatalytic systems with enhanced solar light utilization, *J. Mol. Liq.*, 2022, **357**, 119105.

23 Y. Geng, D. Chen, N. Li, Q. Xu, H. Li, J. He and J. Lu, Z-Scheme 2D/2D α-Fe_2O_3/g-C_3N_4 heterojunction for photocatalytic oxidation of nitric oxide, *Appl. Catal., B*, 2021, **280**, 119409.

24 P. Sarkar, S. De and S. Neogi, Microwave assisted facile fabrication of dual Z-scheme g- C_3N_4/$ZnFe_2O_4$/Bi_2S_3 photocatalyst for peroxymonosulphate mediated degradation of 2, 4, 6-Trichlorophenol: the mechanistic insights, *Appl. Catal., B*, 2022, **307**, 121165.

25 W. Muhammad, W. Alib, M. A. Khan, F. Ali, A. Zada, M. Z. Ansar and P. Yap, Construction of visible-light-driven 2D/2D

$NiFe_2O_4$/g-C_3N_4 Z-scheme heterojunction photocatalyst for effective degradation of organic pollutants and CO_2 reduction, *J. Environ. Chem. Eng.*, 2024, **12**, 113409.

26 S. Mishra and R. Acharya, Recent updates in modification strategies for escalated performance of Graphene/ MFe_2O_4 heterostructured photocatalysts towards energy and environmental applications, *J. Alloys Compd.*, 2023, **960**, 170576.

27 X. Li, H. Xing, X. Yang, D. Wang, J. Feng, Y. Zong, X. Zhu, X. Li and X. Zheng, Construction of $ZnFe_2O_4$/g-C_3N_4 heterojunction as reusable visible-light photocatalyst and the boosted photocatalytic efficiency by photo-self-Fenton effect for organic pollutant degradation, *J. Mater. Sci.: Mater. Electron.*, 2023, **34**, 1204.

28 Z. Dai, Y. Zhen, Y. Sun, L. Li and D. Ding, $ZnFe_2O_4$/g-C_3N_4 S-scheme photocatalyst with enhanced adsorption and photocatalytic activity for uranium(VI) removal, *Chem. Eng. J.*, 2021, **415**, 129002.

29 B. Zhu, B. Chengb, J. Fanc, W. Hod and J. Yu, g-C3N4-based 2D/2D composite heterojunction photocatalyst, *Small Struct.*, 2021, **2**, 2100086.

30 J. Low, S. Cao, J. Yu and S. Wageh, Two-dimensional layered composite photocatalysts, *Chem. Commun.*, 2014, **50**, 10768.

31 X. Zhanga, X. Yuan, L. Jiang, J. Zhang, H. Yu, H. Wang and G. Zeng, Powerful combination of 2D g-C_3N_4 and 2D nanomaterials for photocatalysis: Recent advances, *Chem. Eng. J.*, 2020, **390**, 124475.

32 Q. Chen, L. Wu, J. Wu, K. Ma, W. Ma, W. Wu, F. Guan, P. Li, D. Liu and X. Yang, 2D/2D heterojunction of MgAlTi-LDH/g-C_3N_4 with oxygen vacancy engineering for enhanced photocatalytic activities under natural sunlight, *J. Environ. Chem. Eng.*, 2024, **12**, 112806.

33 Y. Qin, H. Li, J. Lu, Y. Feng, F. Meng, C. Ma, Y. Yan and M. Meng, Synergy between van der Waals heterojunction and vacancy in $ZnIn_2S_4$/g-C_3N_4 2D/2D photocatalysts for enhanced photocatalytic hydrogen evolution, *Appl. Catal., B*, 2020, **277**, 119254.

34 S. Kumaravel, D. S. Lee, T. Niyitang, S. Kaliyamoorthy, I. Hasan and K. Balu, Development of 2D/2D h-MoO_3/Ag/ g-C_3N_4 heterojunction photocatalyst with enhanced photocatalytic performance for the detoxification of methylene blue and tetracycline under solar light illumination, *J. Alloys Compd.*, 2024, **994**, 174666.

35 Z. Wen, H. Ren, D. Li, X. Lu, W. Joo and J. Huang, A highly efficient acetone gas sensor based on 2D porous $ZnFe_2O_4$ nanosheets, *Sens. Actuat. B Chem.*, 2023, **379**, 133287.

36 L. Han, X. Zhou, L. Wan, Y. Deng and S. Zhan, Synthesis of $ZnFe_2O_4$ nanoplates by succinic acid-assisted hydrothermal route and their photocatalytic degradation of rhodamine B under visible light, *J. Environ. Chem. Eng.*, 2014, **2**, 123–130.

37 Z. Wen, H. Ren, D. Li, X. Lu, S. W. Joo and J. Huang, A highly efficient acetone gas sensor based on 2D porous $ZnFe_2O_4$ nanosheets, *Sens. Actuator, B*, 2023, **379**, 133287.

38 H. Jiang, H. Wang and X. Wang, Facile and mild preparation of fluorescent ZnO nanosheets and their bioimaging applications, *Appl. Surf. Sci.*, 2011, **257**, 6991–6995.

39 Q. Wang, G. Chen and H. Yin, New insights into the growth mechanism of hierarchical architectures of PbTe synthesized through a triethanolamine-assisted solvothermal method and their shape-dependent electrical transport properties, *J. Mater. Chem. A*, 2013, **1**, 15355.

40 K.-H. Chen, C.-H. Huang, C.-C. Hsiang, C.-Y. Wu, Y.-H. Yen and Y.-C. Chou, Control of Oxygen Vacancies of 2D-InO_x Fabricated by Liquid Metal Printing via Temperature Modulation, *J. Phys. Chem. C*, 2024, **128**, 5355–5365.

41 Y. Zhu, X. Liu, S. Jin, H. Chen, W. Lee, M. Liu and Y. Chen, Anionic defect engineering of transition metal oxides for oxygen reduction and evolution reactions, *J. Mat. Chem. A.*, 2019, **7**, 5875–5897.

42 L. Acharya, G. Swain, B. P. Mishra, R. Acharya and K. Parida, Development of $MgIn_2S_4$ Microflower-Embedded Exfoliated B-Doped g-C_3N_4 Nanosheets: p–n Heterojunction Photocatalysts toward Photocatalytic Water Reduction and H_2O_2 Production under Visible-Light Irradiation, *ACS Appl. Energy Mater.*, 2022, **5**, 2838–2852.

43 L. Acharya, B. P. Mishra, S. P. Pattnaik, R. Acharya and K. Parida, Incorporating nitrogen vacancies in exfoliated B-doped g-C_3N_4 towards improved photocatalytic ciprofloxacin degradation and hydrogen evolution, *New J. Chem.*, 2022, **46**, 3493–3503.

44 P. Ma, X. Zhang, C. Wang, Z. Wang, K. Wang, Y. Feng, J. Wang, Y. Zhai, J. Deng, L. Wang and K. Zheng, Band alignment of homojunction by anchoring CN quantum dots on g-C3N4 (0D/2D) enhance photocatalytic hydrogen peroxide evolution, *Appl. Catal., B*, 2022, **300**, 120736.

45 T. B. Nguyen, C. Huang and R.-A. Doong, Photocatalytic degradation of bisphenol A over a $ZnFe_2O_4$/TiO_2 nanocomposite under visible light, *Sci. Total Environ.*, 2019, **646**, 745–756.

46 P. Pipattanaporn, P. Pansiri, P. Kumpeerakij, S. Yaemphutchong, P. Siri-apai, N. Suetrong, K. Chansaenpak, S. Singkammo, P. Kanjanaboos, Y. Hanlumyuang, S. Wannapaiboon and W. Wattanathana, Effect of triethanolamine chelating agent on crystallinities, phase purities, and optical properties of zinc aluminate spinel synthesized by thermal decomposition, *Ceram. Int.*, 2022, **48**, 8186–8195.

47 L. T. T. Nguyen, A. T. T. Duong, N. D. Bui, V. T. M. Ngo, H. Q. Nguyen, H. T. T. Nguyen, G. T. Tranc and T. V. Tran, Synthesis of magnetic $NiFe_2O_4$/g-C_3N_4 heterojunction photocatalysts for boosting dye degradation performance under visible-light irradiation, *Nanoscale Adv.*, 2025, **7**, 536–548.

48 Y. Li, Y. Li, X. Xu, C. Ding, N. Chen, H. Ding and A. Lu, Structural disorder controlled oxygen vacancy and photocatalytic activity of spinel-type minerals: A case study of $ZnFe_2O_4$, *Chem. Geol.*, 2018, **504**, 276–287.

49 A. Afzal, A. Mujahid, N. Iqbal, U. Y. Qazi and R. Javaid, Enhanced high-temperature (600 °C) NO_2 Response of $ZnFe_2O_4$ nanoparticle-based exhaust gas sensors, *Nanomaterials*, 2020, **10**, 2133.

50 B. Al-Najara, A. Younisa, L. Hazeemb, S. Seharb, S. Rashdanc, M. N. Shaikhd, H. Albuflasaa and N. P. Hankinse, Thermally

induced oxygen related defects in eco-friendly $ZnFe_2O_4$ nanoparticles for enhanced wastewater treatment efficiencies, *Chemosphere*, 2022, **288**, 132525.

51 S. Mishra, L. Acharya, B. Marandi, K. Sanjay and R. Acharya, Boosted photocatalytic accomplishment of 3D/2D hierarchical structured $Bi_4O_5I_2$/g-C_3N_4 p-n type direct Z-scheme heterojunction towards synchronous elimination of Cr(VI) and tetracycline, *Diamond Relat. Mater.*, 2024, **142**, 110834.

52 P. R. Matli, X. Zhou, D. Shiyu and Q. Huang, Fabrication, characterization, and magnetic behavior of porous $ZnFe_2O_4$ hollow microspheres, *Nano Lett.*, 2015, **5**, 53–59.

53 C. Li, Z. Sun, W. Zhang, C. Yu and S. Zheng, Highly efficient g-C_3N_4/TiO_2/kaolinite composite with novel three-dimensional structure and enhanced visible light responding ability towards ciprofloxacin and S. aureus, *Appl. Catal., B*, 2018, **220**, 272–282.

54 S. Wang and J. Wang, Magnetic 2D/2D oxygen doped g-C_3N_4/biochar composite to activate peroxymonosulfate for degradation of emerging organic pollutants, *J. Hazard. Mater.*, 2022, **423**, 127207.

55 J. Wang, Y. Wang, X. Xv, Y. Chen, X. Yang, J. Zhou, S. Li, F. Cao and G. Qin, Defective Fe^{3+} self-doped spinel $ZnFe_2O_4$ with oxygen vacancies for highly efficient photoelectrochemical water splitting, *Dalton Trans.*, 2019, **48**, 11934.

56 X. Wang, J. Li, K. Chen, J. Li, Y. Jia, Q. Mei and Q. Wang, Facile synthesis of oxygen vacancies enriched $ZnFe_2O_4$ for effective photocatalytic peroxodisulfate activation, *Sep. Purif. Technol.*, 2022, **303**, 122205.

57 Y. Huang, Y. Yu, Y. Yu and B. Zhang, Oxygen Vacancy Engineering in Photocatalysis, *Sol. RRL*, 2020, **4**, 2000037.

58 S. Peng, M. Dan, F. Guo, H. Wang and Y. Li, Template synthesis of $ZnIn_2S_4$ for enhanced photocatalytic H_2 evolution using triethanolamine as electron donor, *Colloids Surf., A*, 2016, **504**, 18–25.

59 P. Guan, P. Han, B. Yang, H. Yin, J. Liu and S. Yang, Rational design of 2D/2D $ZnIn_2S_4$/g-C_3N_4 heterojunction photocatalysts for enhanced photocatalytic H_2 production, *New J. Chem.*, 2023, **47**, 6583–6590.

60 S. Das, S. Paramanik, R. G. Nair and A. Chowdhury, Rational design of mesoporous $ZnFe_2O_4$@g-C_3N_4 heterojunctions for environmental remediation and hydrogen evolution, *Chem. – Eur. J.*, 2024, **30**, e202402512.

61 B. Pan, W. Chen, L. Zhou, X. Lai, J. Qin and C. Wang, $CoFe_2O_4$/carbon nitride Z-scheme heterojunction photocatalytic PMS activation for efficient tetracycline degradation: Accelerated electron transfer, *Process Saf. Environ. Prot.*, 2024, **191**, 2522–2532.

62 J. Guo, L. Shi, L. Wu, S. Pan, X. Yuan and J. Zhao, Spin-polarized electron transport in highly reduced $MgFe_2O_{4-\delta}$, *Mater. Res. Express*, 2018, **5**, 126301.

63 H. Yaghoubi, Z. Li, Y. Chen, H. T. Ngo, V. R. Bhethanabotla, B. Joseph, S. Ma, R. Schlaf and A. Takshi, Toward a visible light-driven photocatalyst: the effect of midgap states-induced energy gap of undoped TiO_2 Nanoparticles, *ACS Catal.*, 2015, **5**, 327–335.

64 M. Dagar, S. Kumar, A. Jain, A. Vohra, M. Singh, J. Dalal, S. Kumar and S. Kaushal, Synergistic Ce/Ag/N-doped ZnO–MWCNT nanocomposites for efficient photocatalytic wastewater remediation with visible light, *Mater. Adv.*, 2025, **6**, 4522–4537.

65 I. N. Reddya, V. Manjunathb and J. Shim, Structural and optical properties, electrochemical impedance spectroscopy, and Mott–Schottky analysis of $ZnFe_2O_4$ nanoparticle-decorated V_2O_5 rectangular nanosheets for photoelectrochemical applications, *J. Environ. Chem. Eng.*, 2021, **9**, 106131.

66 K. K. Das, S. Patnaik, S. Mansingh, A. Behera, A. Mohanty, C. Acharya and K. M. Parida, Enhanced photocatalytic activities of polypyrrole sensitized zinc ferrite/graphitic carbon nitride n-n heterojunction towards ciprofloxacin degradation, hydrogen evolution and antibacterial studies, *J. Colloid Interface Sci.*, 2020, **561**, 551–567.

67 J. Yan, B. Chaia, Y. Liu, G. Fan and G. Song, Construction of 3D/2D $ZnFe_2O_4$/g-C_3N_4 S-scheme heterojunction for efficient photo-Fenton degradation of tetracycline hydrochloride, *Appl. Surf. Sci.*, 2023, **607**, 155088.

68 L. Liu, X. Luo, Y. Li, F. Xu, Z. Gao, X. Zhang, Y. Song, H. Xu and H. Li, Facile synthesis of few-layer g-C_3N_4/ZnO Composite Photocatalyst for Enhancing Visible Light Photocatalytic Performance of Pollutants Removal, *Coll. Surf. A, Physicochem. Eng. Asp.*, 2018, **537**, 516–523.

69 L. Li, W. Jianhua and H. Fang, Fabrication of $ZnFe_2O_4$@g-C_3N_4 for enhanced photo-Fenton effect and visible light-driven organic dye degradation, *Sci. Rep.*, 2025, **15**, 21707.

70 H. Liu, Z. Jin, Z. Xu, Z. Zhang and D. Ao, Fabrication of $ZnIn_2S_4$–g-C_3N_4 sheet-on-sheet nanocomposites for efficient visible-light photocatalytic H_2-evolution and degradation of organic pollutants, *RSC Adv.*, 2015, **5**, 97951–97961.

71 Z. Cui, X. Kuang, R. Lv, X. Jin, F. Chen, Y. Kang, H. Zhang, H. Duan and B. Cao, K-doping g-C_3N_4 with $ZnIn_2S_4$ to construct Z-scheme heterojunction for photocatalytic hydrogen production and dye degradation, *Mater. Res. Bull.*, 2025, **192**, 113580.

72 Z. Xu, B. Xu, K. Qian, Z. Li, F. Ding, M. Fan, Y. Sun and Y. Gao, In situ growth of CuS nanoparticles on g-C_3N_4 nanosheets for H_2 production and the degradation of organic pollutant under visible-light irradiation, *RSC Adv.*, 2019, **9**, 25638–25646.

73 M. Ismael and M. Wark, Photocatalytic activity of $CoFe_2O_4$/g-C_3N_4 nanocomposite toward degradation of different organic pollutants and their inactivity toward hydrogen production: The role of the conduction band position, *Flatchem*, 2022, **32**, 100337.

74 Y. Wu, H. Wang, W. Tu, Y. Liu, S. Wu, Y. Zen Tan and J. W. Chew, Construction of hierarchical 2D-2D $Zn_3In_2S_6$/fluorinated polymeric carbon nitride nanosheets photocatalyst for boosting photocatalytic degradation and hydrogen production performance, *Appl. Catal., B.*, 2018, **233**, 58.

75 Y. Zang, L. Li, Y. Xu, Y. Zuo and G. Li, Hybridization of brookite TiO_2 with g-C_3N_4: a visible-light-driven photocatalyst for As^{3+} oxidation, MO degradation and water splitting for hydrogen evolution, *J. Mater. Chem. A*, 2014, **2**, 15774–15780.

76 M. Ismael, The photocatalytic performance of the ZnO/g-C_3N_4 composite photocatalyst toward degradation of organic pollutants and its inactivity toward hydrogen evolution: The influence of light irradiation and charge transfer, *Chem. Phy. Lett.*, 2020, **739**, 136992.

77 Y. Bai, D. Gu, Z. Chen, J. He, L. Wu, D. Li and X. Shi, Toward enhancing photocatalytic rate by tunable bandgap and oxygen vacancy on 2D g-C_3N_4/WO_{3-x} Z-Schemeheterojunction nanocomposites, *ACS Appl. Nano Mater.*, 2024, **7**, 17339–17350.

78 Y. Li and J. Wang, 2D/2D Z-scheme WO_3/g-C_3N_4 heterojunctions for photocatalytic organic pollutant degradation and nitrogen fixation, *Mater. Adv.*, 2024, **5**, 749.

79 M. Liu, Y. Quan, M. Feng, C. Ren and Z. Wang, Ball-milling preparation of $ZnFe_2O_4$/AgI nanocomposite with enhanced photocatalytic activity, *RSC Adv.*, 2024, **14**, 31193–31204.

80 X. Wang, S. Wang and K. Qi, and S-y Liu, Photocatalytic/ultrasonic catalytic degradation of antibiotic contaminants and hydrogen production with Ni-Doped $ZnFe_2O_4$/g-C_3N_4 nanocomposites, *ACS Appl. Nano*, 2025, **8**, 8010.

81 T. P. Rugma, B. S. Rishi Krishna, K. P. Kangeyan, N. Bernaurdshaw, A. S. AlArific and S. K. Lakhera, Cu_2NiSnS_4/g-C_3N_4 S-scheme photocatalysts: interfacial surface trap states vs. hydrogen production, Sust, *Energy Fuels*, 2024, **8**, 4461.

82 S. Mojumder, T. Das, S. Monga, P. Bhattacharya, S. Pal, S. Ghosh, S. Bhattacharya and M. Pal, Synergistic effect of ZnO–$ZnFe_2O_4$ hetero structures for enhanced surface catalytic activity in Cr(VI) reduction, green H_2 generation and CO sensing: an experimental study supported by DFT, *Nanoscale*, 2025, **17**, 5941.

83 A. K. Shimi, C. Parvathiraj, S. Kumari, J. Dalal, V. Kumar, S. M. Wabaidur and Z. A. Alothman, Green synthesis of SrO nanoparticles using leaf extract of Albizia julibrissin and its recyclable photocatalytic activity: an eco-friendly approach for treatment of industrial wastewater, *Environ. Sci.: Adv.*, 2022, **1**, 849–861.

84 S. Rohilla, A. Gupta, V. Kumar, S. Kumari, M. Petru, N. Amor, M. T. Noman and J. Dalal, Excellent UV-light triggered photocatalytic performance of ZnO.SiO_2 nanocomposite for water pollutant compound methyl orange dye, *Nanomaterials*, 2021, **11**, 2548.

85 P. Arora, A. Fermah, J. K. Rajput, H. Singh and J. Badhan, Efficient solar light-driven degradation of Congo red with novel Cu-loaded Fe_3O_4@TiO_2 nanoparticles, *Environ. Sci. Pol. Res.*, 2017, **24**, 19546.

86 N. Cyril, J. B. George., L. Joseph and V. P. Sylas, Catalytic degradation of methyl orange and selective sensing of Mercury Ion in aqueous solutions using green synthesized silver nanoparticles from the seeds of Derris trifoliata, *J. Cluster Sci.*, 2019, **30**, 459–468.

87 R. He, K. Cheng, Z. Wei, S. Zhang and D. Xu, Room-temperature in situ fabrication and enhanced photocatalytic activity of direct Z-scheme BiOI/g-C_3N_4 photocatalyst, *Appl. Surf. Sci.*, 2019, **465**, 964–972.

88 W. Zhao, Y. Li, P. Zhao, L. Zhang, B. Dai, J. Xu, H. Huang, Y. He and D. Y. C. Leung, Novel Z-scheme Ag-C_3N_4/SnS_2 plasmonic heterojunction photocatalyst for degradation of tetracycline and H_2 production, *Chem. Eng. J.*, 2021, **405**, 126555.

89 S. Mishra, L. Acharya, S. Sharmila, K. Sanjay and R. Acharya, Designing g-C_3N_4/$NiFe_2O_4$ S-scheme heterojunctions for efficient photocatalytic degradation of Rhodamine B and tetracycline hydrochloride, *Appl. Surf. Sci. Adv.*, 2024, **24**, 100647.

90 G. Pahlevanpour and H. Bashiri, Photocatalytic hydrogen production by Ni/TiO_2 (0.5 wt%): Kinetic Monte Carlo simulation, *J. Taiwan Inst. Chem. Eng.*, 2023, **152**, 105159.